

# A comparative study of micromorphic gradient-extensions for anisotropic damage at finite strains

Tim van der Velden\*, Tim Brepols, Stefanie Reese, Hagen Holthusen

*Institute of Applied Mechanics, RWTH Aachen University,  
Mies-van-der-Rohe-Str. 1, D-52074 Aachen, Germany*

**Abstract.** Modern inelastic material model formulations rely on the use of tensor-valued internal variables. When inelastic phenomena include softening, simulations of the former are prone to localization. Thus, an accurate regularization of the tensor-valued internal variables is essential to obtain physically correct results. Here, we focus on the regularization of anisotropic damage at finite strains. Thus, a flexible anisotropic damage model with isotropic, kinematic, and distortional hardening is equipped with three gradient-extensions using a full and two reduced regularizations of the damage tensor. Theoretical and numerical comparisons of the three gradient-extensions yield excellent agreement between the full and the reduced regularization based on a volumetric-deviatoric regularization using only two nonlocal degrees of freedom.

**Keywords:** Anisotropic damage, localization, micromorphic approach, gradient-extension

## 1 Introduction

**Motivation.** The prediction of complex material phenomena is, nowadays, based on inelastic material models with tensor-valued internal variables for the description of e.g. plasticity, viscoelasticity, anisotropic damage, or growth. Yet, finite element simulations of inelastic phenomena without a regularization method suffer from the occurrence of localization when modeling softening in e.g. plasticity and damage (de Borst et al. [1999]), or viscoelasticity (Steif et al. [1982]). Analogously to Poh et al. [2011] for small strain plasticity, this work is concerned with the open research question of choosing a regularization for tensor-valued internal variables and focuses on the specific inelastic phenomenon of anisotropic damage.

---

\*Corresponding author:

phone: +49 (0) 241 80 25016, fax: +49 (0) 241 80 22001, email: tim.van.der.velden@ifam.rwth-aachen.de

**Anisotropic damage modeling.** Various modeling methodologies have evolved to describe the induced anisotropy due to material degradation. Formulations based on a split of the volumetric (isotropic) and deviatoric (anisotropic) material response that are separately degraded by two scalar damage variables may be found in e.g. Carol et al. [2002], Leukart and Ramm [2003]. Microplane models, see e.g. Carol et al. [1991], Kuhl et al. [2000], project the macroscopic strain state onto different material planes, where unidirectional constitutive laws are evaluated, and afterwards obtain the macroscopic material response by a homogenization process (cf. Leukart and Ramm [2003]). A multiplicative split of the deformation gradient into elastic and damage related components is used by e.g. Voyiadjis and Park [1999], Schütte and Bruhns [2002], and Dorn and Wulfinghoff [2021], where the latter consider the inelastic part to consist out of a normal crack and a shear crack contribution. An effective or fictitious undamaged configuration is introduced by e.g. Menzel et al. [2002], Langenfeld and Mosler [2020], Sprave and Menzel [2023] to formulate the modeling equations. Finally, anisotropic damage can be interpreted as an evolving structural tensor, see e.g. Desmorat et al. [2007] (whose localization properties were investigated in Jirásek and Suárez [2016]), Badreddine et al. [2015], Desmorat [2016], Fassin et al. [2019*b,a*], Reese et al. [2021], Hegde and Mulay [2022], Holthusen et al. [2022*a*], which is also the approach followed in this work.

**Regularization techniques.** To remedy the mesh dependence and localization, different approaches can be pursued to account for a nonlocal behavior. Spatial averaging techniques for a specific quantity are employed in nonlocal integral-type formulations, see e.g. Pijaudier-Cabot and Bažant [1987] for a spatial average of the damage driving variable, Bažant and Pijaudier-Cabot [1988] for a spatial average of the damage variable, and Bažant and Jirásek [2002] for an overview of nonlocal integral-type formulations. Viscous regularization approaches may be found in e.g. Needleman [1988], Geers et al. [1994], Niazi et al. [2013], Langenfeld et al. [2018] and peridynamics based formulations that are inherently nonlocal in e.g. Silling [2000], Javili et al. [2021], Laurien et al. [2023].

Gradient-extended models provide another effective regularization method that incorporate the gradient of a (local) quantity into the formulation. In e.g. Peerlings et al. [1996], the gradient of the equivalent strain and, in de Borst et al. [1996], the gradient of an internal variable are considered. Moreover, the gradient-extension of an anisotropic microplane damage model is presented in Kuhl et al. [2000]. A decisive advancement for gradient-extended material models with respect to their straightforward model incorporation is associated with the works of Dimitrijevic and Hackl [2008, 2011] and Forest [2009, 2016], who introduce a nonlocal counterpart for the local variable, which is to be regularized. The gradient effects act on the nonlocal field and the coupling between the local variable and its nonlocal counterpart is achieved by a penalty approach. Thereby, the local material model formulation is equipped with an additional driving force, but remains otherwise unaltered, which is from the authors' point of view an elegant incorporation of the nonlocal character.

**Current and future works.** The search for efficient gradient-extension of tensor-valued internal variables is an active field of research and not restricted to anisotropic damage, but also for e.g. plasticity still an open question. After the works of e.g. Wulfinghoff and Böhlke [2012], Wulfinghoff et al. [2015] for strain gradient plasticity, novel scalar-based gradient plasticity models are presented in Jebahi and Forest [2021], Abatour et al. [2023], and Abatour and Forest [2023]. Further, Friedlein et al. [2023] compare different gradient-extensions in the logarithmic strain space for plasticity coupled to damage. Moreover, gradient-extensions for fiber-reinforced materials are presented by e.g. Holthusen et al. [2020], Poggenpohl et al. [2021] and the search for gradient-extended scale-transitions at severe material softening by Poggenpohl et al. [2022]. In Langenfeld et al. [2022], three different regularization concepts for brittle damage are compared and, in Sprave and Menzel [2023], gradient-extensions for anisotropic damage and plasticity at finite strains are investigated.

Following the search for a reduced and effective gradient-extension, the model should then be incorporated into structural elements (e.g. Aldakheel et al. [2019], Barfusz et al. [2021b, 2022], Kikis et al. [2021]) to avoid locking and be combined with a multiphysical framework (e.g. Dittmann et al. [2020], Sarkar et al. [2020], van der Velden et al. [2021, 2023]) for holistic production and process simulations. Furthermore, an incorporation of the reduced gradient-extension into the novel iCANN-framework of Holthusen et al. [2023] is aspired.

**Outline of the work.** In Section 2, the constitutive modeling framework of the anisotropic damage model is elaborated for a general gradient-extension. Then, in Section 3, three specific gradient-extensions are motivated and compared theoretically. Thereafter, in Section 4, the three gradient-extended models are applied to four structural examples and compared with respect to the structural responses and the resulting damage patterns. Finally, a conclusion is presented in Section 5.

**Notational conventions.** In this work, italic characters  $a$ ,  $A$  denote scalars and zeroth-order tensors and bold-face italic characters  $\mathbf{b}$ ,  $\mathbf{B}$  refer to first- and second-order tensors. The operators  $\text{Div}(\bullet)$  and  $\text{Grad}(\bullet)$  denote the divergence and gradient operation of a quantity with respect to the reference configuration.  $\mathbf{A} \cdot$  defines the single contraction and  $\mathbf{a} :$  the double contraction of two tensors. The time derivative of a quantity is given by  $(\dot{\bullet})$ .

## 2 Constitutive modeling

In this Section 2, we briefly present the brittle model version of Holthusen et al. [2022a] without specification of its gradient-extension. The core and novelty part of this paper, i.e. the choice and comparison of different gradient-extensions, is discussed in detail in Section 3.

## 2.1 Strong and weak forms

The gradient-extension in this work is incorporated following the micromorphic approach of Forest [2009, 2016] using a nonlocal micromorphic tuple (see Holthusen et al.[2022a]). Thus, the balance of linear momentum, stated in the reference configuration, reads

$$\text{Div}(\mathbf{F}\mathbf{S}) + \mathbf{f}_0 = \mathbf{0} \quad \text{in } \Omega_0 \quad (1)$$

$$\mathbf{F}\mathbf{S} \cdot \mathbf{n}_0 = \mathbf{t}_0 \quad \text{on } \Gamma_{t0} \quad (2)$$

$$\mathbf{u} = \mathbf{u}' \quad \text{on } \Gamma_{u0} \quad (3)$$

and, furthermore, the balance of the micromorphic field reads

$$\text{Div}(\Xi_{0_i} - \Xi_{0_e}) - \xi_{0_i} + \xi_{0_e} = \mathbf{0} \quad \text{in } \Omega_0 \quad (4)$$

$$(\Xi_{0_i} - \Xi_{0_e}) \cdot \mathbf{n}_0 = \xi_{0_c} \quad \text{on } \Gamma_{c0} \quad (5)$$

$$\bar{\mathbf{d}} = \bar{\mathbf{d}}' \quad \text{on } \Gamma_{\bar{\mathbf{d}}0} \quad (6)$$

with the primary variables being the displacement  $\mathbf{u}$  and the nonlocal micromorphic tuple  $\bar{\mathbf{d}}$ . Moreover,  $\mathbf{F}$  denotes the deformation gradient,  $\mathbf{S}$  the Second Piola-Kirchhoff stress,  $\mathbf{f}_0$  the mechanical volume forces,  $\mathbf{n}_0$  the outward normal vector,  $\mathbf{t}_0$  the applied mechanical surface tractions,  $\xi_{0_i}$  and  $\Xi_{0_i}$  the internal forces related to the micromorphic tuple and its gradient,  $\xi_{0_e}$  and  $\Xi_{0_e}$  the micromorphic volume forces, and  $\xi_{0_c}$  the micromorphic tractions. Boundary conditions for the primary variables are generally denoted by  $(\bullet)'$ . However, since  $\Gamma_{\bar{\mathbf{d}}0} = \emptyset$  is employed, for the micromorphic boundary conditions  $\Gamma = \Gamma_{c0}$  holds.

Using the test functions  $\delta\mathbf{u}$  and  $\delta\bar{\mathbf{d}}$ , the strong forms, Eqs. (1)-(6), are transferred to their corresponding weak forms under the assumption of a simplified micromorphic balance equation, i.e. neglecting external and contact forces as well as Dirichlet boundary conditions for the micromorphic tuple, resulting in

$$g_u(\mathbf{u}, \bar{\mathbf{d}}, \delta\mathbf{u}) := \int_{\Omega_0} \mathbf{S} : \delta\mathbf{E} \, dV - \int_{\Omega_0} \mathbf{f}_0 \cdot \delta\mathbf{u} \, dV - \int_{\Gamma_{t0}} \mathbf{t}_0 \cdot \delta\mathbf{u} \, dA = 0, \quad (7)$$

$$g_{\bar{\mathbf{d}}}(\mathbf{u}, \bar{\mathbf{d}}, \delta\bar{\mathbf{d}}) := \int_{\Omega_0} \xi_{0_i} \cdot \delta\bar{\mathbf{d}} \, dV + \int_{\Omega_0} \Xi_{0_i} : \text{Grad}(\delta\bar{\mathbf{d}}) \, dV = 0. \quad (8)$$

Finally, for the linearization and finite element discretization the reader is kindly referred to Holthusen et al.[2022a].

## 2.2 Kinematics

The constitutive framework is based on logarithmic strains and, thereby, facilitates a physically motivated formulation of the elastic energy contribution that distinguishes between isochoric and volumetric damage mechanisms in the finite strain regime considering the damage growth



criterion of Wulfinghoff et al. [2017]. Analogously to e.g. Miehe et al. [2002], the logarithmic strain is defined as

$$\boldsymbol{\eta} := \frac{1}{2} \ln(\boldsymbol{C}) \quad (9)$$

where  $\boldsymbol{C}$  denotes the right Cauchy-Green deformation tensor.

In contrast to the additive split used in finite strain plasticity, see e.g. Holthusen et al.[2022a] for ductile damage with logarithmic strains, which is only exactly valid for coaxial loadings, the consideration of solely brittle damage does not rely on kinematic approximations and, hence, the framework in this work is geometrically exact.

### 2.3 Thermodynamically consistent derivation

The model's total Helmholtz free energy  $\psi$  is additively split into four contributions

$$\psi(\boldsymbol{\eta}, \boldsymbol{D}, \xi_d, \mathbf{d}, \bar{\mathbf{d}}, \text{Grad}(\bar{\mathbf{d}})) = \psi_e(\boldsymbol{\eta}, \boldsymbol{D}) + \psi_d(\xi_d) + \psi_h(\boldsymbol{D}) + \psi_{\bar{d}}(\mathbf{d}, \bar{\mathbf{d}}, \text{Grad}(\bar{\mathbf{d}})) \quad (10)$$

where  $\psi_e$  represents the elastic energy depending on the strain  $\boldsymbol{\eta}$  and the second-order damage tensor  $\boldsymbol{D}$ . Next,  $\psi_d$  represents the isotropic damage hardening energy depending on the accumulated damage variable  $\xi_d$ . The additional kinematic damage hardening energy  $\psi_h$  (cf. Hansen and Schreyer [1994]) ensures that the eigenvalues of the damage tensor are limited to a value of one and that complete failure is described by  $\boldsymbol{D} = \boldsymbol{I}$  (see Fassin et al. [2019b,a], Holthusen et al.[2022a]). Finally,  $\psi_{\bar{d}}$  represents the micromorphic energy contribution depending on a general local tuple  $\mathbf{d} := (d_1, \dots, d_{n_{\bar{d}}})$ , a set of  $n_{\bar{d}}$  local invariants formulated in terms of the damage tensor  $\boldsymbol{D}$ , and as a corresponding counterpart the nonlocal micromorphic tuple  $\bar{\mathbf{d}} := (\bar{d}_1, \dots, \bar{d}_{n_{\bar{d}}})$  and its gradient  $\text{Grad}(\bar{\mathbf{d}})$ .

Following a general derivation in this section, the specific forms of the energies are presented in Section 2.4.

The isothermal Clausius-Duhem inequality including the micromorphic extension reads (cf. Forest [2009, 2016])

$$-\dot{\psi} + \boldsymbol{\alpha} : \dot{\boldsymbol{\eta}} + \xi_{0_i} \cdot \dot{\bar{\mathbf{d}}} + \boldsymbol{\Xi}_{0_i} : \text{Grad}(\dot{\bar{\mathbf{d}}}) \geq 0 \quad (11)$$

where the stress power is given in terms of the logarithmic strain rate  $\dot{\boldsymbol{\eta}}$  and its thermodynamically conjugate force  $\boldsymbol{\alpha}$ .

The rate of the Helmholtz free energy, Eq. (10), is computed with respect to the rates of its arguments as

$$\dot{\psi} = \frac{\partial \psi}{\partial \boldsymbol{\eta}} : \dot{\boldsymbol{\eta}} + \frac{\partial \psi}{\partial \boldsymbol{D}} : \dot{\boldsymbol{D}} + \frac{\partial \psi}{\partial \xi_d} \dot{\xi}_d + \frac{\partial \psi}{\partial \mathbf{d}} \cdot \dot{\mathbf{d}} + \frac{\partial \psi}{\partial \text{Grad}(\bar{\mathbf{d}})} : \text{Grad}(\dot{\bar{\mathbf{d}}}). \quad (12)$$

Please note, that the partial derivative of the energy  $\psi$  with respect to the damage tensor  $\boldsymbol{D}$  yields the elastic, the additional damage hardening and the nonlocal damage driving forces  $\boldsymbol{Y}_e$ ,

$\mathbf{Y}_h$ , and  $\mathbf{Y}_{\bar{d}}$  that are defined as

$$\frac{\partial \psi}{\partial \mathbf{D}} = \underbrace{\frac{\partial \psi_e}{\partial \mathbf{D}}}_{=:-\mathbf{Y}_e} + \underbrace{\frac{\partial \psi_h}{\partial \mathbf{D}}}_{=:\mathbf{Y}_h} + \underbrace{\frac{\partial \psi_{\bar{d}}}{\partial \mathbf{D}}}_{=:\mathbf{Y}_{\bar{d}}} =: -\mathbf{Y}. \quad (13)$$

In Section 3, we will present and compare the explicit forms of the nonlocal damage driving force  $\mathbf{Y}_{\bar{d}}$ , since these differ for distinct choices of the micromorphic tuple, i.e. the gradient-extension, whilst the other damage driving forces  $\mathbf{Y}_e$  and  $\mathbf{Y}_h$  remain unchanged.

Thereafter, the rates of Eq. (12) are inserted into the balance equation, Eq. (11), and yield by repositioning

$$\begin{aligned} & \left( \boldsymbol{\alpha} - \frac{\partial \psi}{\partial \boldsymbol{\eta}} \right) : \dot{\boldsymbol{\eta}} + \underbrace{(\mathbf{Y}_e - \mathbf{Y}_h - \mathbf{Y}_{\bar{d}})}_{=:\mathbf{Y}} : \dot{\mathbf{D}} + R_d \dot{\xi}_d \\ & + \left( \boldsymbol{\xi}_{0_i} - \frac{\partial \psi}{\partial \bar{\mathbf{d}}} \right) \cdot \dot{\bar{\mathbf{d}}} + \left( \boldsymbol{\Xi}_{0_i} - \frac{\partial \psi}{\partial \text{Grad}(\bar{\mathbf{d}})} \right) : \text{Grad}(\dot{\bar{\mathbf{d}}}) \geq 0. \end{aligned} \quad (14)$$

**State laws.** The state laws are obtained by the Coleman and Noll [1961] procedure and the argumentation of Forest [2016] as

$$\boldsymbol{\alpha} = \frac{\partial \psi}{\partial \boldsymbol{\eta}}, \quad (15)$$

$$\boldsymbol{\xi}_{0_i} = \frac{\partial \psi}{\partial \bar{\mathbf{d}}}, \quad (16)$$

$$\boldsymbol{\Xi}_{0_i} = \frac{\partial \psi}{\partial \text{Grad}(\bar{\mathbf{d}})} \quad (17)$$

and the reduced dissipation inequality with  $R_d := -\partial \psi / \partial \xi_d$  as

$$\mathbf{Y} : \dot{\mathbf{D}} + R_d \dot{\xi}_d \geq 0. \quad (18)$$

**Evolution equations.** For the evolution of the internal variables  $\mathbf{D}$  and  $\xi_d$ , we define two general convex, zero-valued, and non-negative inelastic potentials  $g_{d_1}$  and  $g_{d_2}$  in terms of the driving forces  $\mathbf{Y}$  and  $R_d$  that yield the evolution equations

$$\dot{\mathbf{D}} = \dot{\gamma}_d \frac{\partial g_{d_1}}{\partial \mathbf{Y}}, \quad (19)$$

$$\dot{\xi}_d = \dot{\gamma}_d \frac{\partial g_{d_2}}{\partial R_d} \quad (20)$$

where  $\dot{\gamma}_d$  is the damage multiplier which is obtained by satisfying the damage onset criterion  $\Phi_d(\mathbf{Y}, R_d) \leq 0$  in accordance with the Karush-Kuhn-Tucker conditions

$$\dot{\gamma}_d \geq 0, \quad \Phi_d \leq 0, \quad \dot{\gamma}_d \Phi_d = 0. \quad (21)$$

## 2.4 Specific forms of Helmholtz free energy, damage onset criterion and inelastic potentials

**Helmholtz free energy.** Motivated by e.g. Desmorat [2016], Badreddine et al. [2015], Leukart and Ramm [2003], Lemaitre et al. [2000] and similar to Simo [1987], the elastic energy features a physically motivated split into isochoric and volumetric parts to account for the evolution of micro cracks and microvoids separately. Moreover, it fulfills the damage growth criterion (Wulfinghoff et al. [2017]) and reads

$$\psi_e = \mu \operatorname{tr}(\operatorname{dev}(\boldsymbol{\eta})^2 (\mathbf{I} - \mathbf{D})) \vartheta + f_d \mu \operatorname{tr}(\operatorname{dev}(\boldsymbol{\eta})^2) (1 - \vartheta) + f_d \frac{K}{2} \operatorname{tr}(\boldsymbol{\eta})^2 \quad (22)$$

with the isotropic degradation function

$$f_d = \left(1 - \frac{\operatorname{tr}(\mathbf{D})}{3}\right)^{e_d} \quad (23)$$

where  $\mu$  denotes the elastic shear modulus,  $\kappa$  the elastic bulk modulus,  $\vartheta$  the degree of damage anisotropy, and  $e_d$  the exponent of the isotropic degradation function. Nonlinear and linear isotropic damage hardening are incorporated by

$$\psi_d = r_d \left( \xi_d + \frac{\exp(-s_d \xi_d) - 1}{s_d} \right) + \frac{1}{2} H_d \xi_d^2 \quad (24)$$

with the damage hardening parameters  $r_d$ ,  $s_d$  and  $H_d$ . The additional kinematic damage hardening energy is formulated in terms of the eigenvalues  $D_i$  of the damage tensor

$$\psi_h = K_h \sum_{i=1}^3 \left( -\frac{(1 - D_i)^{1 - \frac{1}{n_h}}}{1 - \frac{1}{n_h}} - D_i + \frac{1}{1 - \frac{1}{n_h}} \right) \quad (25)$$

where  $K_h$  and  $n_h$  are numerical parameters. The micromorphic energy contribution penalizes the difference between the components of the local and the nonlocal tuple by the numerical penalty parameters  $H_i$  and incorporates an internal length scale via the gradient of the nonlocal quantity and the materials parameters  $A_i$  for each component of the micromorphic tuple up to the total number of nonlocal degrees of freedom  $n_{\bar{d}}$

$$\psi_{\bar{d}} = \frac{1}{2} \sum_{i=1}^{n_{\bar{d}}} H_i (d_i - \bar{d}_i)^2 + \frac{1}{2} \sum_{i=1}^{n_{\bar{d}}} A_i \operatorname{Grad}(\bar{d}_i) \cdot \operatorname{Grad}(\bar{d}_i). \quad (26)$$

**Damage onset criterion.** The chosen damage onset criterion with damage threshold  $Y_0$

$$\Phi_d := \sqrt{3} \sqrt{\mathbf{Y}_+ : \mathbb{A} : \mathbf{Y}_+} - (Y_0 - R_d) \leq 0 \quad (27)$$

features the option to include distortional damage hardening with the fourth order interaction tensor  $\mathbb{A}$  and material parameter  $c_d$

$$\mathbb{A} = ((\mathbf{I} - \mathbf{D})^{c_d} \otimes (\mathbf{I} - \mathbf{D})^{c_d})^{\frac{23}{T}} \quad (28)$$

with the positive semi-definite part of the damage driving force being

$$\mathbf{Y}_+ = \sum_{i=1}^3 \langle Y_i \rangle \mathbf{n}_i^Y \otimes \mathbf{n}_i^Y \quad (29)$$

where  $\langle \bullet \rangle = \max(\bullet, 0)$ .

**Inelastic potentials.** The inelastic potential  $g_{d_1}$  for the evolution of the damage tensor is chosen in a pseudo-non-associative structure as

$$g_{d_1} = \frac{3}{2(Y_0 - R_d)} \mathbf{Y}_+ : \mathbb{A} : \mathbf{Y}_+ \quad (30)$$

where the relation  $\sqrt{3} \sqrt{\mathbf{Y}_+ : \mathbb{A} : \mathbf{Y}_+} = Y_0 - R_d$  obtained from Eq. (27) for a converged state is utilized to avoid a division by zero in the local iteration (cf. Challamel et al. [2005], Holthusen et al. [2022a]), when algorithmic differentiation (e.g. Korelc [2002], Korelc and Wriggers [2016]) is employed. However, the absolute value and direction of the evolution are identical to choosing an associative evolution equation, i.e.  $\dot{\mathbf{D}} = \partial \Phi_d / \partial \mathbf{Y}$ . Furthermore, the inelastic potential  $g_{d_2}$  for the evolution of the accumulated damage is chosen linearly as

$$g_{d_2} = R_d. \quad (31)$$

## 3 Micromorphic gradient-extensions

### 3.1 Motivation

The novelty of this work lies in the comparison of different gradient-extensions for anisotropic damage with respect to their efficiency and accuracy. To ensure the comparability of the results, the same local anisotropic damage formulation is utilized throughout this work and only the choice of the local micromorphic tuple, i.e. the selection of local quantities whose localization is prevented by the gradient-extensions, is adapted. Here, we restrict ourselves to invariant-based micromorphic tuples of the damage tensor and are, thus, able to study the effect of different nonlocal damage driving forces.

Other authors, e.g. Fassin et al. [2019b,a], Sprave and Menzel [2023], investigated the regularization of a scalar damage hardening variable. However, as pointed out by Fassin et al. [2019b], this procedure can violate the differentiability of the damage onset function when employing associative damage evolution by maximizing the dissipation and is, thus, not considered in this context.

In the following, we present three model formulations (models A, B, and C) with full, using six nonlocal degrees of freedom, and reduced regularization of the damage tensor, using three and two nonlocal degrees of freedom.

Initially, we strive for a rigorous regularization of the damage tensor and, therefore, in model A, all six independent components of the symmetric second order damage tensor are regularized individually. Thereby, no localization is expected to occur and, furthermore, an accurate reference solution for the reduced regularizations is obtained. A similar procedure can be found in Langenfeld and Mosler [2020], where the six independent components of the integrity tensor are regularized. However, a full regularization requires six additional nonlocal micromorphic degrees of freedom and, thus, triples the number of global degrees of freedom compared to the local, purely mechanical problem. Due to this significant increase in degrees of freedom, we aim to reduce the former and to simultaneously maintain the regularization's accuracy.

The idea for the first reduced regularization is based on the uniqueness of the eigenvalues of the damage tensor. A regularization of the former should, thus, also lead to a proper regularization of the entire tensor. For the ease of numerical implementation and since the principal traces of the damage tensor can unambiguously determined from its eigenvalues, model B utilizes the reduced micromorphic tuple of Holthusen et al.[2022a]. In this formulation, the micromorphic tuple contains the three principal traces of the damage tensor to each of which a corresponding nonlocal counterpart is introduced. Compared to model A, model B requires three nonlocal degrees of freedom less, but still doubles the total number of degrees of freedom compared to the local model.

We, therefore, aim to achieve a further reduction in the required number of nonlocal degrees of freedom and motivate a regularization of the volumetric and deviatoric part of the damage tensor based on two nonlocal degrees of freedom. Since isotropic damage yields by its nature and the sole consideration of microvoids a volumetric damage tensor  $D\mathbf{I}$  and requires only a single nonlocal degree of freedom, we aim to capture the damage anisotropy due to the micro cracks by a regularization of the deviatoric part of the damage tensor as is has been suggested for investigation in Holthusen et al.[2022b]. A further advantage of model C becomes apparent when considering isotropic damage, since only one nonlocal degree of freedom is non-zero whereas for model A and B still three nonlocal degrees of freedom are non-zero.

### 3.2 Specific micromorphic tuples

To ensure all models' objectivity, the micromorphic tuples are formulated based on invariants of the damage tensor. For the micromorphic tuple of model A, we introduce six general structural tensors  $M_1, M_2, M_3, M_4, M_5$ , and  $M_6$  that yield

$$\mathbf{d}^A = (\text{tr}(DM_1), \text{tr}(DM_2), \text{tr}(DM_3), \text{tr}(DM_4), \text{tr}(DM_5), \text{tr}(DM_6)) . \quad (32)$$

In order to control the normal and shear components of the damage tensor, we specify the structural tensors according to the Cartesian basis vectors  $\mathbf{e}_1$ ,  $\mathbf{e}_2$ , and  $\mathbf{e}_3$  as

$$\begin{aligned}\mathbf{M}_1 &= \mathbf{e}_1 \otimes \mathbf{e}_1, \mathbf{M}_2 = \mathbf{e}_2 \otimes \mathbf{e}_2, \mathbf{M}_3 = \mathbf{e}_3 \otimes \mathbf{e}_3, \\ \mathbf{M}_4 &= \mathbf{e}_1 \otimes \mathbf{e}_2, \mathbf{M}_5 = \mathbf{e}_1 \otimes \mathbf{e}_3, \mathbf{M}_6 = \mathbf{e}_2 \otimes \mathbf{e}_3.\end{aligned}\quad (33)$$

The micromorphic tuple based on the principal traces of the damage tensor of model B stems from Holthausen et al.[2022a] and reads

$$\mathbf{d}^B = (\text{tr}(\mathbf{D}), \text{tr}(\mathbf{D}^2), \text{tr}(\mathbf{D}^3)). \quad (34)$$

Finally, the micromorphic tuple of model C with a split of the damage tensor into volumetric and deviatoric part reads

$$\mathbf{d}^C = \left( \frac{\text{tr}(\mathbf{D})}{3}, \text{tr}(\text{dev}(\mathbf{D})^2) \right). \quad (35)$$

### 3.3 Explicit nonlocal damage driving forces

Next, we compare the explicit forms of the nonlocal damage driving forces that are derived from  $\mathbf{Y}_{\bar{d}} = \partial \psi_{\bar{d}} / \partial \mathbf{D}$ . Their general form depends on the number of elements per micromorphic tuple  $n_{\bar{d}}$  and reads

$$\mathbf{Y}_{\bar{d}} = \sum_{i=1}^{n_{\bar{d}}} H_i (d_i - \bar{d}_i) \frac{\partial d_i}{\partial \mathbf{D}}. \quad (36)$$

The explicit form of the nonlocal damage driving force of model A reads under the consideration of the symmetry of  $\mathbf{D}$

$$\begin{aligned}\mathbf{Y}_{\bar{d}}^A &= H_1 (\text{tr}(\mathbf{D}\mathbf{M}_1) - \bar{d}_1) \text{sym}(\mathbf{M}_1) \\ &+ H_2 (\text{tr}(\mathbf{D}\mathbf{M}_2) - \bar{d}_2) \text{sym}(\mathbf{M}_2) \\ &+ H_3 (\text{tr}(\mathbf{D}\mathbf{M}_3) - \bar{d}_3) \text{sym}(\mathbf{M}_3) \\ &+ H_4 (\text{tr}(\mathbf{D}\mathbf{M}_4) - \bar{d}_4) \text{sym}(\mathbf{M}_4) \\ &+ H_5 (\text{tr}(\mathbf{D}\mathbf{M}_5) - \bar{d}_5) \text{sym}(\mathbf{M}_5) \\ &+ H_6 (\text{tr}(\mathbf{D}\mathbf{M}_6) - \bar{d}_6) \text{sym}(\mathbf{M}_6).\end{aligned}\quad (37)$$

With  $\partial \text{tr}(\mathbf{D}^i) / \partial \mathbf{D} = i \mathbf{D}^{i-1}$ , the explicit form for model B reads

$$\begin{aligned}\mathbf{Y}_{\bar{d}}^B &= H_1 (\text{tr}(\mathbf{D}) - \bar{d}_1) \mathbf{I} \\ &+ H_2 (\text{tr}(\mathbf{D}^2) - \bar{d}_2) 2\mathbf{D} \\ &+ H_3 (\text{tr}(\mathbf{D}^3) - \bar{d}_3) 3\mathbf{D}^2.\end{aligned}\quad (38)$$

And using  $\text{dev}(\mathbf{D}) = \mathbf{D} - \text{tr}(\mathbf{D})/3 \mathbf{I}$ , the explicit form for model C reads

$$\begin{aligned} \mathbf{Y}_{\bar{d}}^C = & \frac{H_1}{3} \left( \frac{\text{tr}(\mathbf{D})}{3} - \bar{d}_1 \right) \mathbf{I} \\ & + H_2 \left( \text{tr}(\text{dev}(\mathbf{D})^2) - \bar{d}_2 \right) \left( 2\mathbf{D} - \frac{2}{3} \text{tr}(\mathbf{D}) \mathbf{I} \right) \end{aligned} \quad (39)$$

When comparing the damage driving forces of model A, B, and C, Eqs.(37)-(39), their different structures are evident and, thus, also for identical choices of the parameters  $H_1, \dots, H_{n_{\bar{d}}}$  and  $A_1, \dots, A_{n_{\bar{d}}}$  different model responses are to be expected.

## 4 Numerical examples

The aim of this section is to study the interesting research question whether an accurate regularization of anisotropic damage models can efficiently be obtained by a reduced regularization of the damage tensor. Therefore, we investigate four representative structural examples by utilizing models A, B, and C and are, thus, able to identify the effect of the gradient-extension with the simulation of the very same boundary value problem with different models. Further, we can directly compare the accuracy of the reduced regularizations (models B and C) to the reference solution with full regularization (model A).

The material point behavior of the anisotropic damage model was examined in detail in Holthusen et al.[2022a] to which we kindly refer the interested reader for further information. The generic material parameters are, unless stated otherwise, adopted from Brepols et al. [2020] and Holthusen et al.[2022a] and listed in Table 1. For each example, the internal length scales  $A_i$  of models A and C were identified such that the maximum force of the structural response coincided with the one obtained by model B. The Taylor series sampling point  $a_h$  listed in Table 1 is required for the implementation of the kinematic damage driving force (cf. Holthusen et al.[2022a]), but was omitted in the model presentation in Section 2. In order to avoid snap-backs during the simulation, an artificial viscosity  $\eta_v$  is utilized. Comprehensive studies in Sections 4.1 and 4.2 confirm that the results are unaffected by the artificial viscosity for a choice of  $\eta_v = 1$  [MPa s]. The two-dimensional examples in Sections 4.1, 4.2 and 4.4 utilize four-node quadrilateral plane-strain elements and the three-dimensional example in Section 4.3 utilizes eight-node hexahedral elements.

The finite element simulations were conducted using the software *FEAP* (Taylor and Govindjee [2020]), new finite element meshes for the example of Section 4.4 were created with the software *HyperMesh* (HyperWorks [2022]), and post-processing of the simulations' results was carried out with *ParaView* (Ahrens et al. [2005]).

Table 1: Material and numerical parameters

Symbol	Material parameter	Value	Unit
$\mu$	Elastic shear modulus	55000	MPa
$K$	Elastic bulk modulus	61666.6	MPa
$\vartheta$	Damage anisotropy	0 / 1	-
$e_d$	Isotropic degradation function exponent	1	-
$Y_0$	Initial damage threshold	2.5	MPa
$c_d$	Distortional hardening exponent	1	-
$H_d$	Linear isotropic hardening prefactor	1	MPa
$r_d$	Nonlinear isotropic hardening prefactor	5	MPa
$s_d$	Nonlinear isotropic hardening scaling factor	100	-
$K_h$	Kinematic hardening prefactor	0.1	MPa
$n_h$	Kinematic hardening exponent	2	-
$A_i$	Internal length scales	75 - 1300	MPa mm <sup>2</sup>

Symbol	Numerical parameter	Value	Unit
$a_h$	Taylor series sampling point	0.999999	-
$H_i$	Micromorphic penalty parameters	10 <sup>4</sup>	MPa
$\eta_v$	Artificial viscosity	1	MPa s



## 4.1 Plate with hole specimen

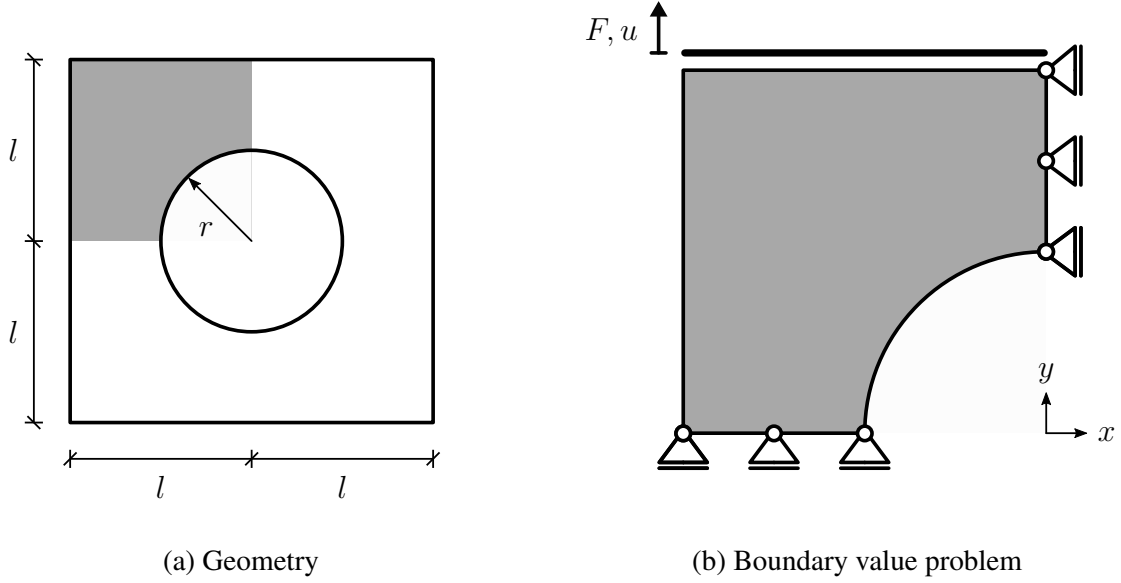


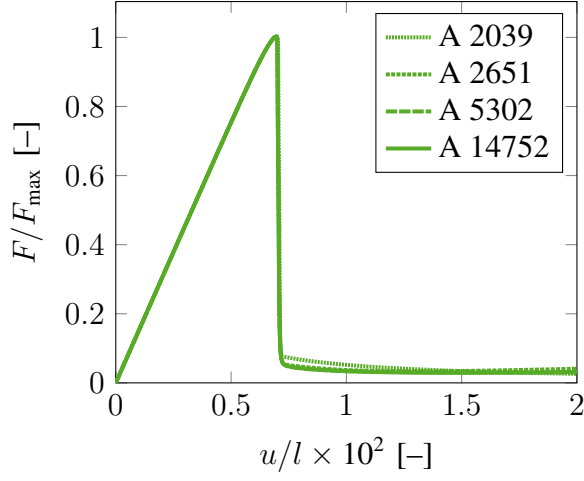
Figure 1: Geometry and boundary value problem of the plate with hole specimen.

The first example is characterized by a tension dominated loading situation and considers a plate with hole specimen. This example was, in the context of isotropic damage, previously investigated by e.g. Friedlein et al. [2021], Sprave and Menzel [2020], Kiefer et al. [2018], Brepols et al. [2017], Dimitrijevic and Hackl [2008] and, for anisotropic damage, by e.g. Sprave and Menzel [2023], Langenfeld and Mosler [2020], Fassin et al. [2019b].

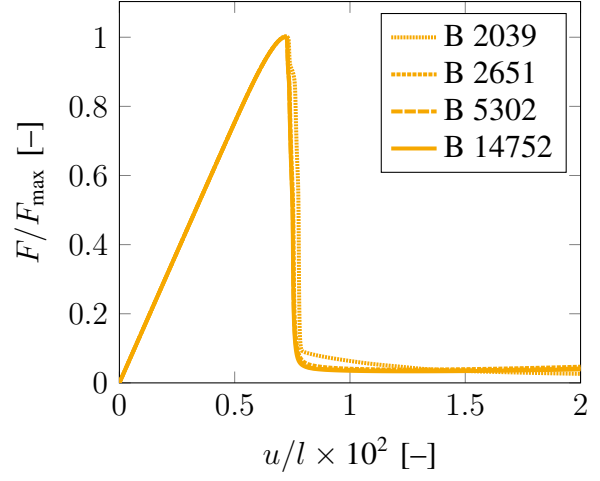
Fig. 1 shows the geometry and the considered boundary value problem. The dimensions read  $l = 100$  [mm] and  $r = 50$  [mm] with a thickness of 1 [mm]. Due to symmetry, only one quarter of the specimen is modeled in the simulation and the top edge is moved in vertical direction by a prescribed displacement. The finite element meshes stem from Fassin et al. [2019b]. The internal length scales of model B are chosen as  $A_i^B = 75$  [MPa mm<sup>2</sup>] and the parameters of model A and C are identified as  $A_i^A = 420$  [MPa mm<sup>2</sup>] and  $A_i^C = 1300$  [MPa mm<sup>2</sup>].

In Fig. 2, the normalized force-displacement curves prove mesh convergence for all models already upon the first refinement with 2651 elements (see Figs. 2a - 2c). Furthermore, Fig. 2d provides the direct comparison of all models using the finest mesh with 14752 elements. Model A and C yield an identical structural response, while the vertical force drop of model B is shifted to the right with  $u_{0.5 F_{\max}}^B = 0.751$  [mm] compared to  $u_{0.5 F_{\max}}^{A,C} = 0.706$  [mm].

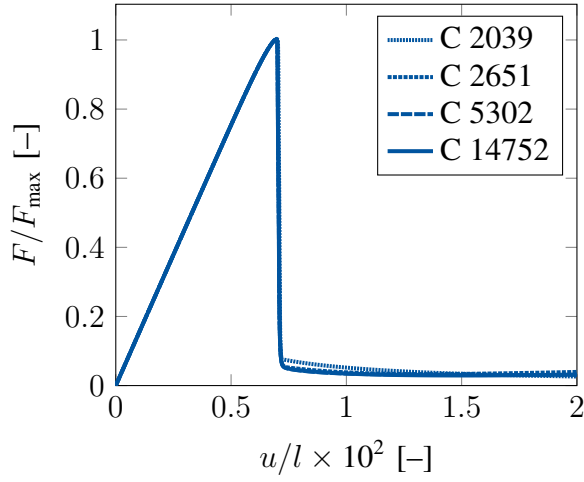
Fig. 3 shows the damage contour plots at the end of the simulation. For all models, the width of the damage zone of component  $D_{yy}$  is thicker than that of component  $D_{xx}$ , since the specimen is loaded in  $y$ -direction. Models A and C yield coinciding results, whilst for model B, the damage zone for both normal components of the damage tensor are more pronounced. This



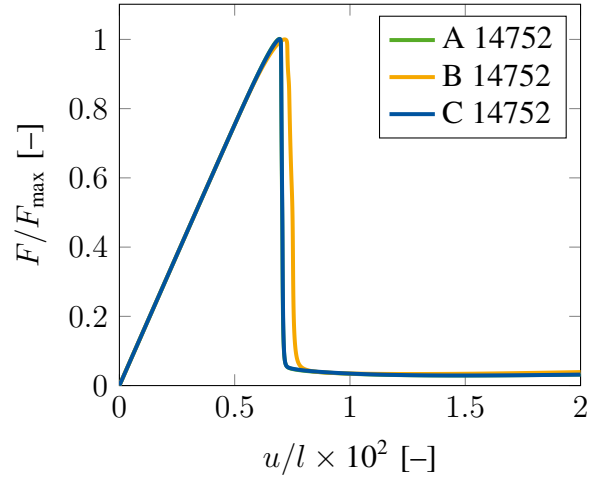
(a) Model A



(b) Model B



(c) Model C



(d) Model comparison

Figure 2: Mesh convergence studies for the plate with hole specimen and model comparison. The forces are normalized with respect to the maximum force of the finest mesh (14752 elements) of model B with  $F_{\max} = 5.0767 \times 10^4$  [N].

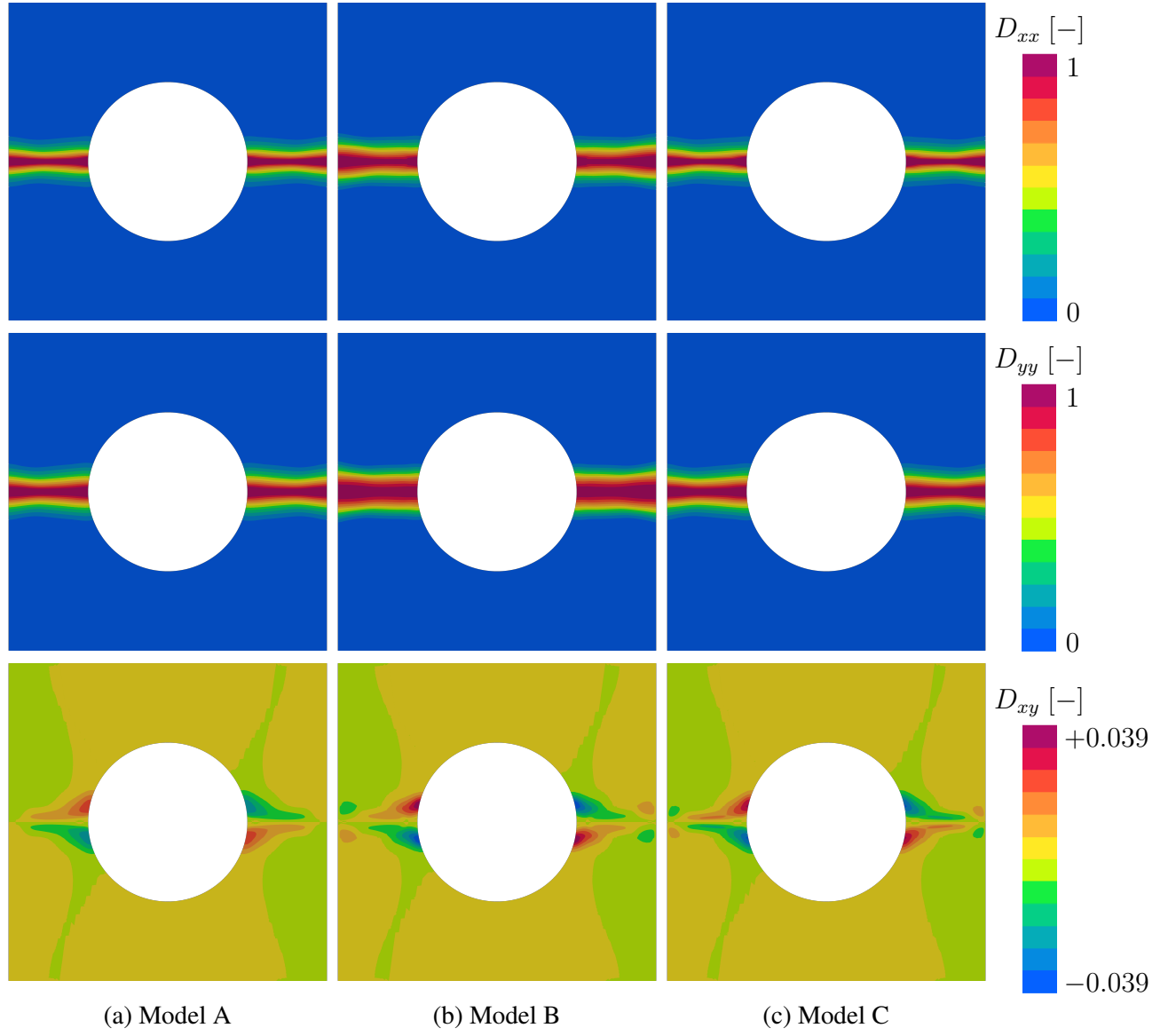


Figure 3: Contour plots of the normal and shear components of the damage tensor for the plate with hole specimen at the end of the simulation.

observation is consistent with the results of Fig. 2d, where, loosely speaking, the area under the force-displacement curve is larger for model B and, hence, a larger amount of energy is dissipated in this case, which implies that the corresponding damage zones have to be larger as well.

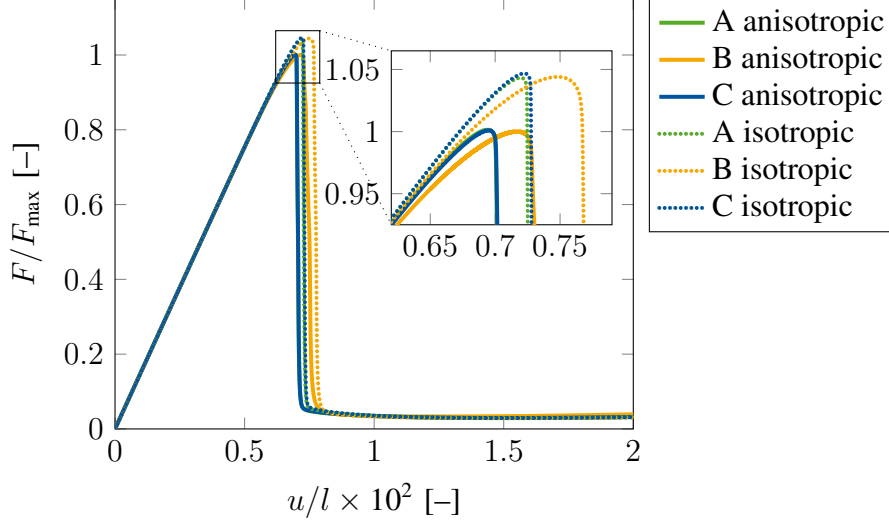


Figure 4: Comparison of the force-displacement curves of the anisotropic and isotropic computation for the plate with hole specimen (14752 elements). The forces are normalized with respect to the maximum force of the anisotropic computation of model B with  $F_{\max} = 5.0767 \times 10^4$  [N].

Next, we examine the necessity of using an anisotropic damage formulation, here i.e.  $\vartheta = 1$  [–], compared to an isotropic one, i.e.  $\vartheta = 0$  [–]. Fig. 4 shows the force-displacement curves of the plate with hole simulation with the finest mesh (14752 elements) for all models using the anisotropic and isotropic model formulation. Evidently, the isotropic damage formulations continuously overestimate the structure’s maximum load bearing capacity (A: +4.18 [%], B: +4.26 [%], C: +4.58 [%]). Deviations in the resulting damage contour plots for anisotropic and isotropic damage can also be observed in Fig. 5, where the shape and intensity are clearly nonconforming at the edges of the damage zone.

Then, we investigate the behavior of the local model formulation without utilizing a gradient-extension, analogously to Fassin et al. [2019b], in order to ensure that no regularizing effects result from the use of an artificial viscosity. Fig. 6 shows the force-displacement curves for different mesh-discretizations and, as clearly indicated by the enlarged image section, no convergence with respect to the maximum force can be observed upon mesh refinement. This observation suggests the occurrence of localization in the simulation, which is confirmed by the damage contour plots in Fig. 7, where the crack localizes into a single row of elements for each mesh. From the results of Figs. 6 and 7 we can infer that the consideration of a sufficiently small artificial viscosity, here  $\eta_v = 1$  [Ns/mm<sup>2</sup>], does not cure the mesh dependence of the

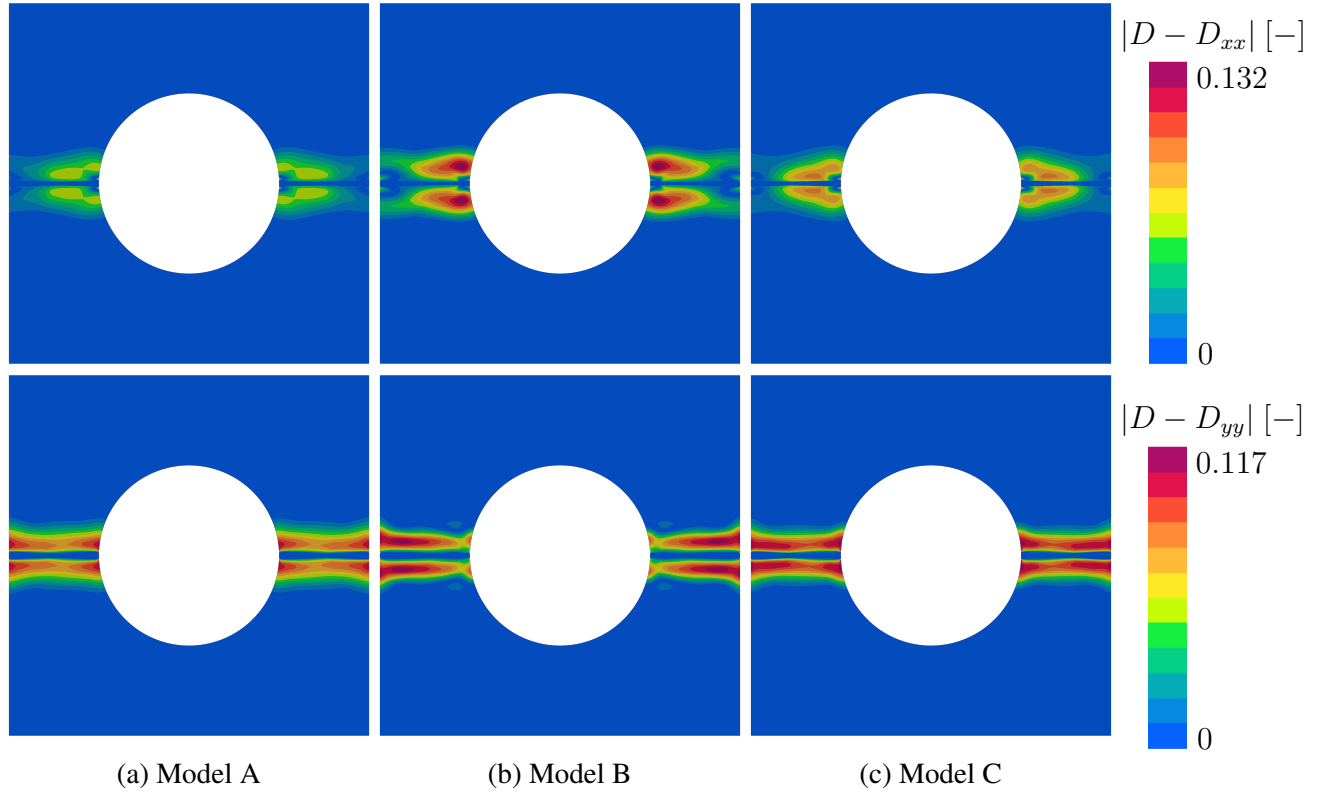


Figure 5: Comparison of the damage contour plots of the anisotropic and isotropic computation for the plate with hole specimen by a difference plot of the isotropic damage value  $D$  compared to the normal components of the anisotropic damage tensor  $D_{xx}$  and  $D_{yy}$ .

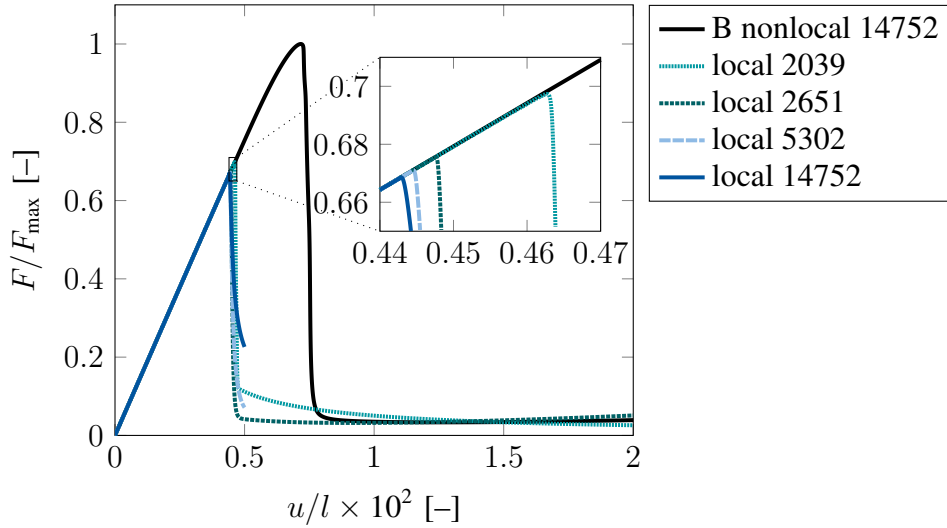


Figure 6: Force-displacement curves for the local damage model without gradient-extension for the plate with hole specimen for increasing degrees of mesh refinement. The forces are normalized with respect to the maximum force of the nonlocal computation of model B with  $F_{\max} = 5.0767 \times 10^4$  [N].

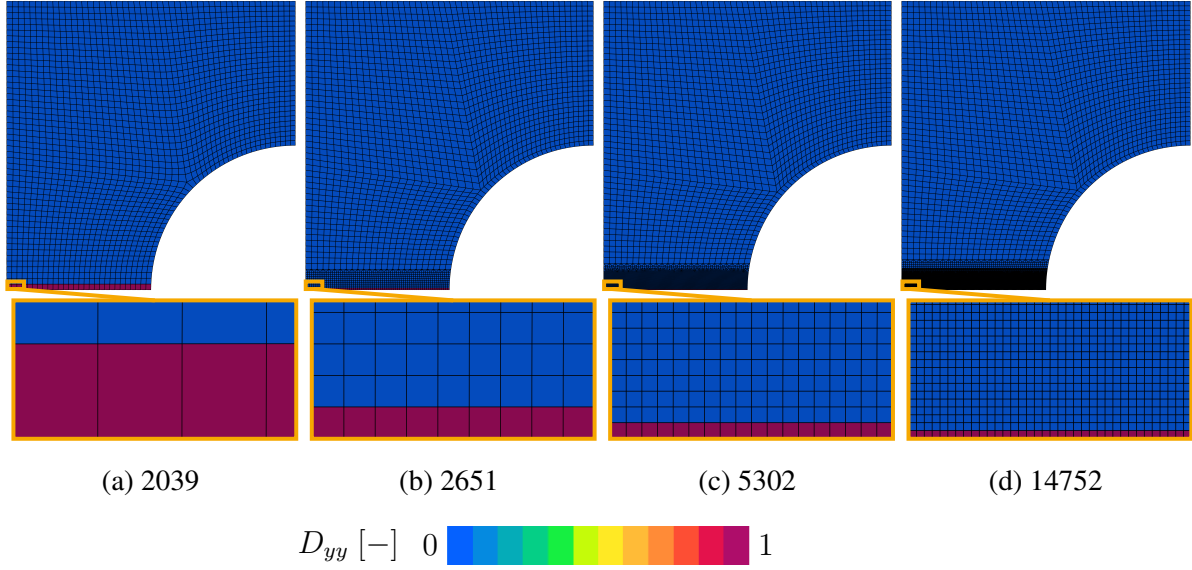


Figure 7: Damage contour plots for the local anisotropic damage model for the plate with hole specimen captured at position  $u/l \times 10^2 = 0.5$  [-] from Fig. 6 for different mesh discretizations. The damage values are averaged over all Gauss-points per element.

local damage model and, thus, does not interfere with the investigated regularizations.

Nevertheless, the model's response is obviously not completely independent of the choice of the artificial viscosity. Thus, we study the influence of the parameter  $\eta_v$  in Figs. 8 and 9 using model C. Fig. 8 shows the increasing the artificial viscosity leads to a less step drop in the force-displacement curve after reaching the maximum peak load and, also, to a higher residual force after the failure of the specimen. However, the maximum load bearing capacity of the structure is unaffected by a variation of  $\eta_v$ . Fig. 9 shows the difference plots for the components of the damage tensor comparing the results of using  $\eta_v = 1$  [Ns/mm<sup>2</sup>] versus  $\eta_v = 2/4/10$  [Ns/mm<sup>2</sup>]. Even for an increase of the artificial viscosity by a factor of ten, the maximum difference for the normal and shear components yields only values of  $|\Delta D_{xx}| = 0.0386$  [-],  $|\Delta D_{yy}| = 0.0395$  [-], and  $|\Delta D_{xy}| = 0.0015$  [-].

These studies have proven the negligible influence of the artificial viscosity on the results of the simulation and justify its use in the present work to allow for a displacement-driven load control.

## 4.2 Asymmetrically notched specimen

The next example compares the three gradient-extensions for a combined tension and shear loading situation and considers an asymmetrically notched specimen. This example has also been investigated in e.g. Friedlein et al. [2023], Felder et al. [2022], Barfusz et al.[2021a], Brepols et al. [2020], Ambati et al. [2016] and also in Holthusen et al.[2022a], where the same

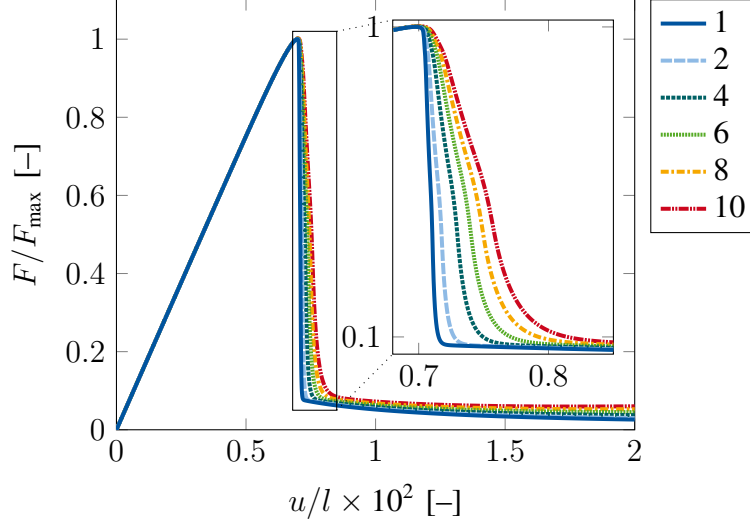


Figure 8: Force-displacement curves for the plate with hole specimen using model C for a variation of the artificial viscosity  $\eta_v$  (mesh 2039). The forces are normalized with respect to the maximum force of  $\eta_v = 1$  [N s/mm<sup>2</sup>] (2039 elements) with  $F_{\max} = 5.0920 \times 10^4$  [N].

boundary value problem with the same material parameters is solved for model B using an arc-length controlled method yielding a double snap-back. These results serve in this section as an additional reference solution for model B and confirm the displacement controlled simulation results using the artificial viscosity.

Fig. 10 shows the geometry and the corresponding boundary value problem. The dimensions read  $h = 36$  [mm],  $l = 100$  [mm],  $l_1 = 40$  [mm],  $l_2 = 20$  [mm] and  $r = 5$  [mm] with a thickness of 1 [mm]. The finite element meshes stem from Felder et al. [2022] and Holthusen et al.[2022a]. The internal length scales of model B are chosen, analogously to Holthusen et al.[2022a], as  $A_i^B = 100$  [MPa mm<sup>2</sup>] and the parameters of model A and C are identified as  $A_i^A = 330$  [MPa mm<sup>2</sup>] and  $A_i^C = 1100$  [MPa mm<sup>2</sup>].

Fig. 11 shows the normalized force-displacement curves for the asymmetrically notched specimen and all models predict the maximum peak force also with the coarsest mesh (1624 elements) accurately. In the post-failure regime, models A and C show with increasing mesh refinement less deviations from the final solution compared to model B (see Figs. 11a-11c). The model comparison in Fig. 11d shows that, analogously to the tension dominated example in Section 4.1, the vertical drop of model B is shifted to the right, i.e.  $u_{0.5 F_{\max}}^B = 1.062$  [mm] compared to  $u_{0.5 F_{\max}}^A = 0.947$  [mm] and  $u_{0.5 F_{\max}}^C = 0.955$  [mm].

In Fig. 12, the damage contour plots with a zoom to the center of the asymmetrically notched specimen are presented. All models demonstrate the formation of a shear crack between the notches as well as a more pronounced evolution of the damage component  $D_{xx}$ , since the  $x$ -direction corresponds to the loading direction. With regard to the normal components of the

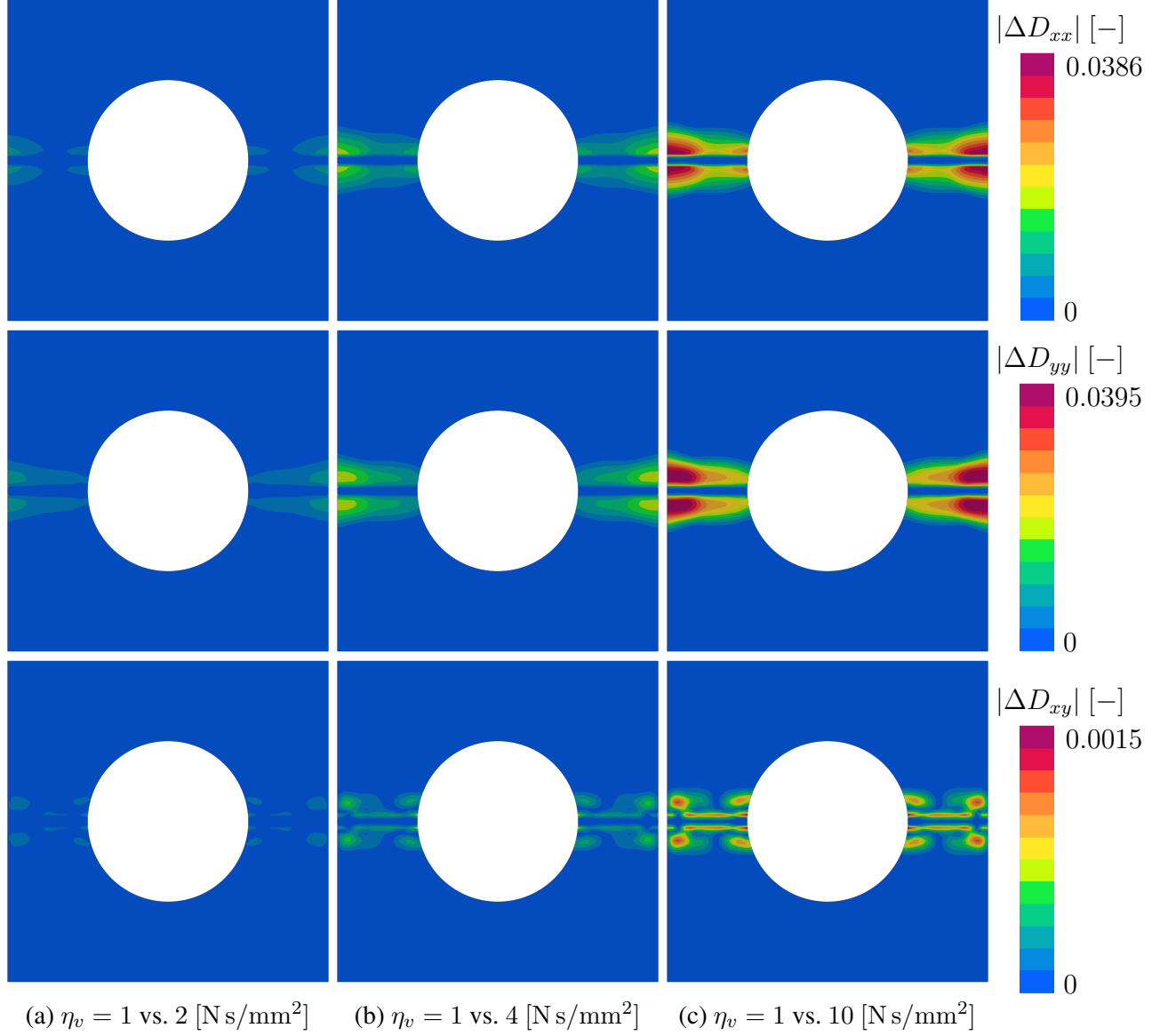
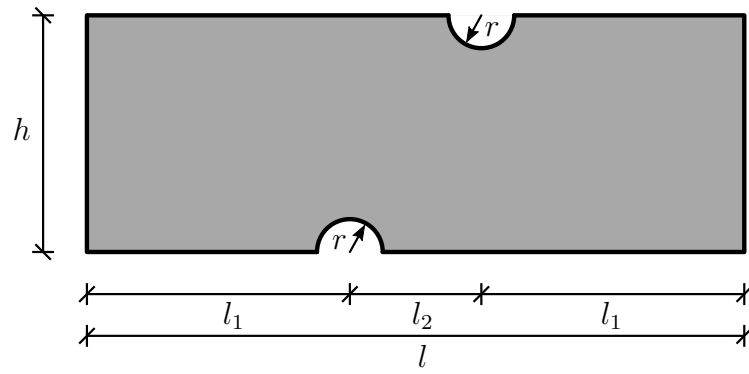
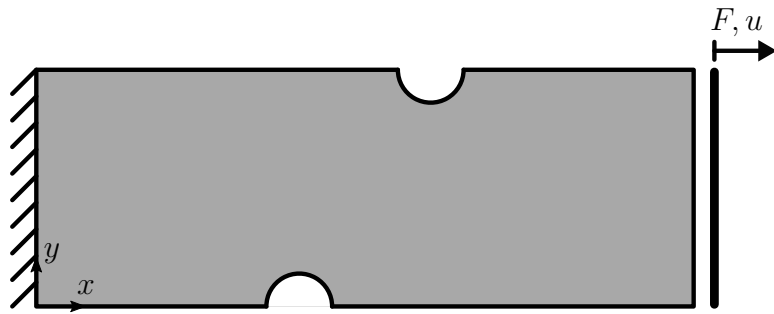


Figure 9: Difference plot of the damage contours of the normal and shear components of the damage tensor for the plate with hole specimen using model C for different values of the artificial viscosity  $\eta_v$  at the end of the simulation of Fig. 8.



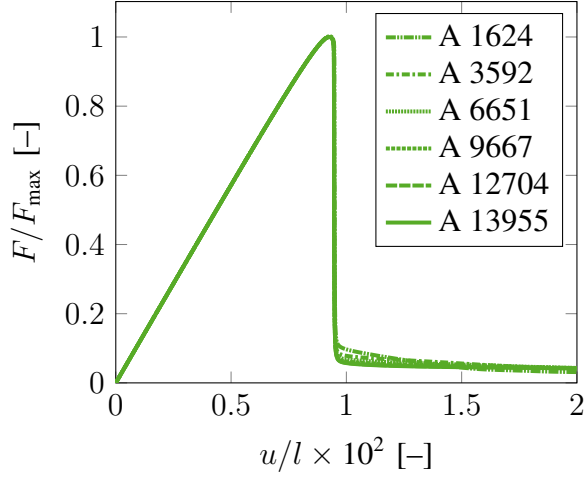


(a) Geometry

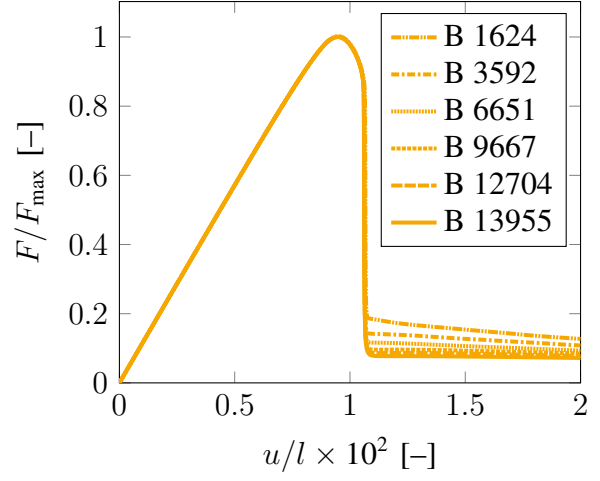


(b) Boundary value problem

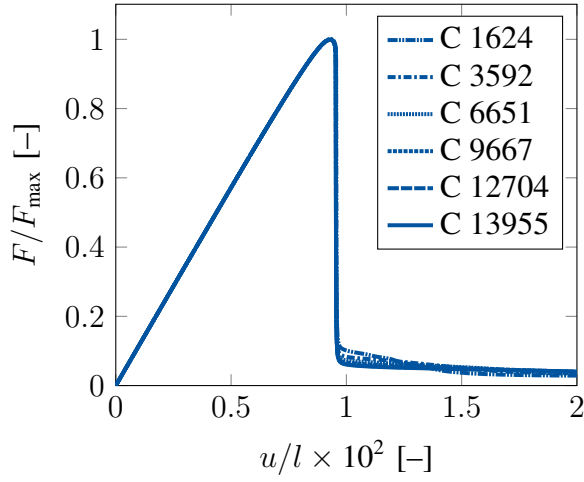
Figure 10: Geometry and boundary value problem of the asymmetrically notched specimen.



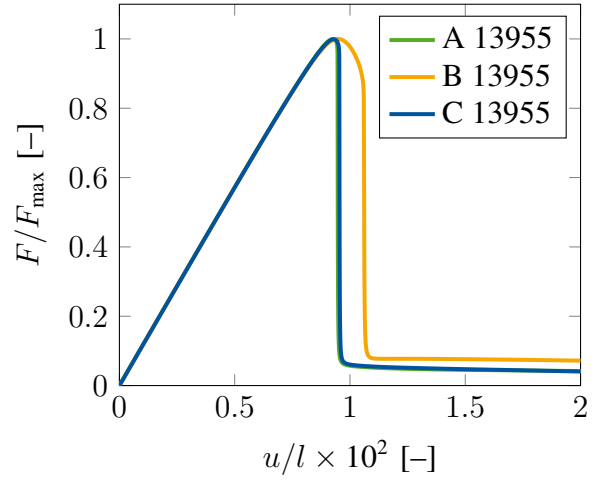
(a) Model A



(b) Model B



(c) Model C



(d) Model comparison

Figure 11: Mesh convergence studies for the asymmetrically notched specimen and model comparison. The forces are normalized with respect to the maximum force of the finest mesh (13955 elements) of model B with  $F_{\max} = 3.7959 \times 10^4$  [N].

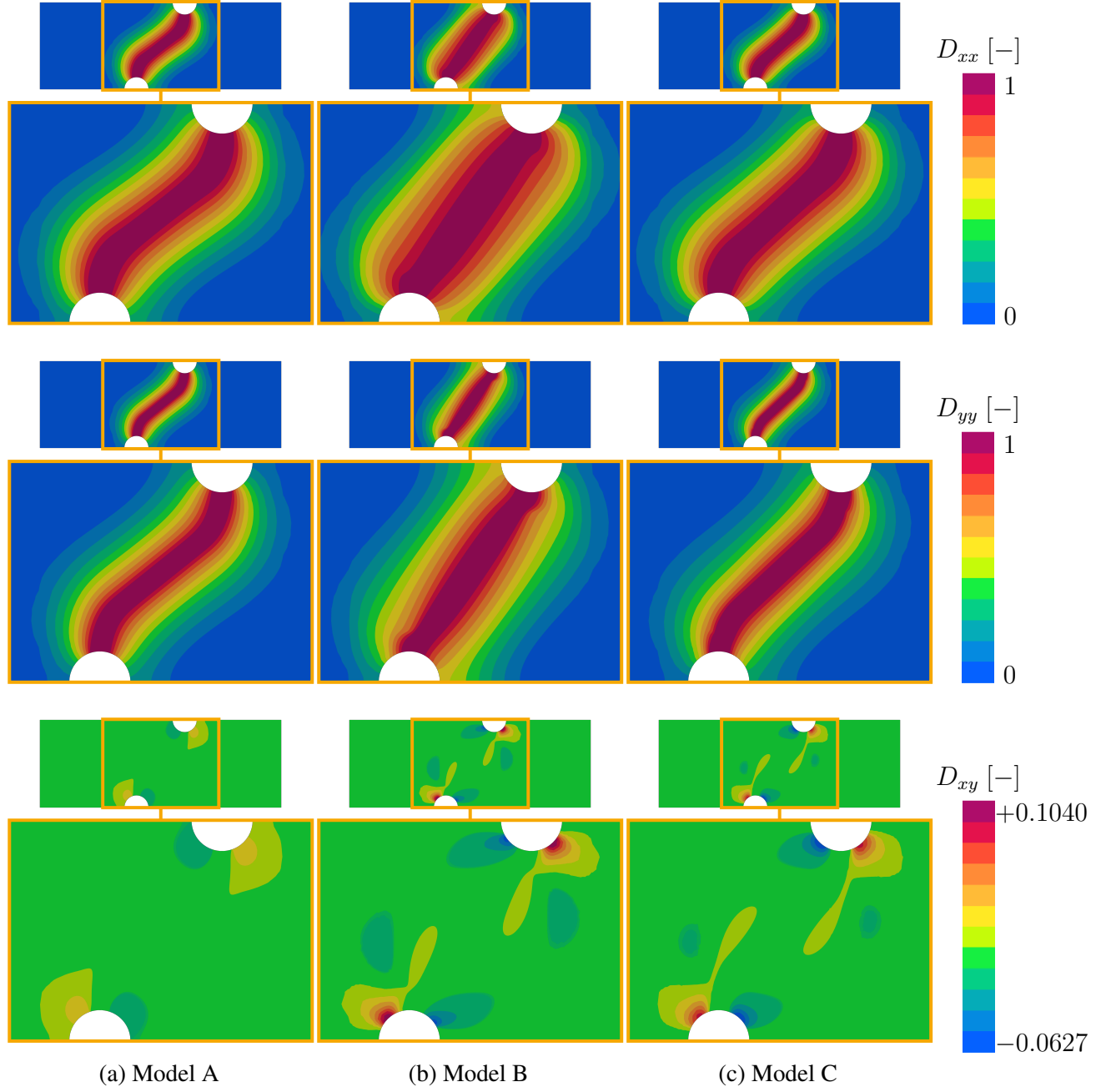


Figure 12: Contour plots of the normal and shear components of the damage tensor for the asymmetrically notched specimen at the end of the simulation.

damage tensor, the results of models A and C differ in shape and intensity compared to model B. While models A and C yield a sigmoidal crack pattern, model B yields a straight shear crack. Moreover, the total width of the damage zone for model B is greater than for models A and C, which is in line with the findings of Section 4.1. When comparing the shear components of the damage tensor, model A yields the evolution of  $D_{xy}$  over a wider spread area compared to models B and C, but exhibits no distinct peak values at the notches. The smoothed out distribution of  $D_{xy}$  can result from the strict regularization properties of model A that controls each component of the damage tensor individually.

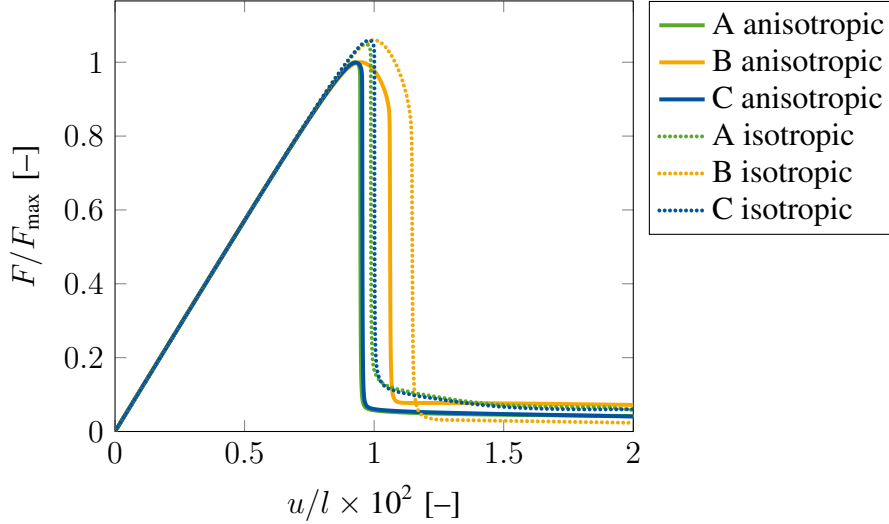


Figure 13: Comparison of the anisotropic and isotropic computation for the asymmetrically notched specimen (13955 elements). The forces are normalized with respect to the maximum force of the anisotropic computation of model B with  $F_{\max} = 3.7959 \times 10^4$  [N].

The study comparing isotropic and anisotropic damage for the asymmetrically notched specimen is presented in Fig. 13. The force-displacement curves yield also for this example a significant overestimation of the maximum peak force when considering only an isotropic damage formulation (A: +4.86 [%], B: +6.00 [%], C: +6.03 [%]) and corroborates that damage has to be modeled as an anisotropic phenomenon.

Finally, this example serves to compare the displacement driven load control using artificial viscosity to an arc-length driven load control without artificial viscosity for model B. Fig. 14 shows the force-displacement curves for both load control procedures, where the arc-length controlled reference solution is obtained from Holthusen et al.[2022a]. Both procedures yield the same maximum peak force also for coarse meshes. Then, the displacement driven procedure yields a vertical drop of the force-displacement curve while the arc-length controlled procedure yields a double snap-back during the force decrease. Thereafter, the curves again unite and are congruent with each other and, thus, proof that both control procedures, with and without artificial viscosity, are equally valid.

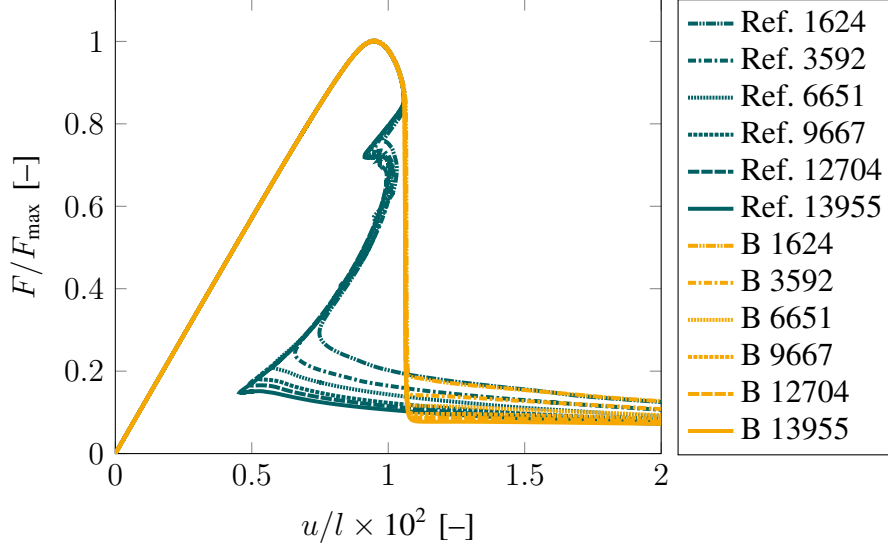


Figure 14: Comparison of the results of model B for the asymmetrically notched specimen obtained by a displacement-controlled procedure using artificial viscosity and by an arc-length controlled procedure (reference solution from Holthusen et al.[2022a]). The forces are normalized with respect to the maximum force of the computation with the displacement-driven procedure (13955 elements) with  $F_{\max} = 3.7959 \times 10^4$  [N].

### 4.3 Three-dimensional tensile specimen

This example features the failure investigation of a three-dimensional I-shaped tensile specimen with models A, B, and C. Previously, this example was investigated in Felder et al. [2022] in the context of thermo-mechanical coupling, in Ambati et al. [2016] numerically and experimentally, and in Holthusen et al. 2022b with a ductile formulation of model B.

Fig. 15 shows the geometry and the considered boundary value problem. Due to symmetry, only an eighth of the original specimen is considered in the simulation. The dimensions read  $l = 50$  [mm],  $h_1 = 10$  [mm],  $h_2 = 6.25$  [mm],  $d = 5$  [mm],  $r = 15$  [mm] and  $t = 1.5$  [mm]. The finite element meshes stem from Holthusen et al. 2022b. The internal length scales of model B are chosen as  $A_i^B = 75$  [MPa mm<sup>2</sup>] and the parameters of model A and C are identified as  $A_i^A = 180$  [MPa mm<sup>2</sup>] and  $A_i^C = 680$  [MPa mm<sup>2</sup>]. In the simulation we apply  $u_t = 2$  [mm] at the end of the specimen and plot in Fig. 16 the reaction force  $F$  over the displacement  $u$  at position  $x = 0$  [mm],  $y = 25$  [mm], and  $z = 0$  [mm] (cf. Fig. 15b).

In Fig. 16, all models again yield in the force-displacement curves the same maximum peak force also for coarse mesh discretizations (580 elements). In this example, only models A and C were able to compute converged solutions up to the final loading of  $u_t = 2$  [mm]. With model B, no solution could be obtained due to local convergence problems beyond  $u_t = 0.556$  [mm], which corresponds to  $u = 0.456$  [mm] and  $u/l \times 10^2 = 0.912$  [-] (see Fig. 16b).

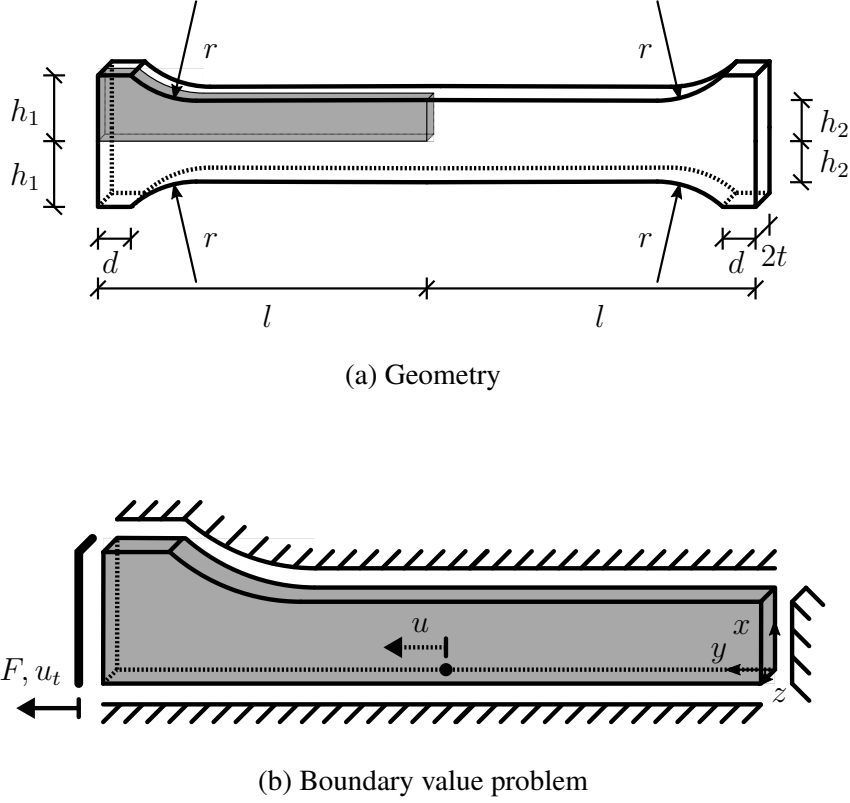


Figure 15: Geometry and boundary value problem of the three-dimensional tensile specimen.

The model comparison in Fig. 16d shows again an excellent agreement between models A and C, while model B analogously to the previous Sections 4.1 and 4.2, yields a higher energy dissipation. The points of comparison for the damage contour plots in Figs. 17 and 18 are indicated by the black boxes in Fig. 16d.

As already reported in Holthusen et al. 2022b, the damage tensor component  $D_{yy}$ , i.e. the degradation of the plane perpendicular to the loading direction evolves most pronounced for all models (see Fig. 17). And again, the damage zone of model B spreads furthest and, thus, dissipates the largest amount of energy. Moreover, the contour plots for the normal components agree well for models A and C.

In Fig. 18, the study of the shear components  $D_{xy}$ , a plane parallel to the loading direction, reveals a concentration at the shoulder of the specimen for all models. The study of the shear components  $D_{xz}$ , i.e. the plane perpendicular to the loading direction, yields a uniform distribution, except for the center of the specimen with model B. The study of the shear components  $D_{yz}$ , i.e. the second plane perpendicular to the loading direction, reveals a localization for model B at the transition from the fine to the coarse mesh, which cannot be observed for the full regularization with model A.

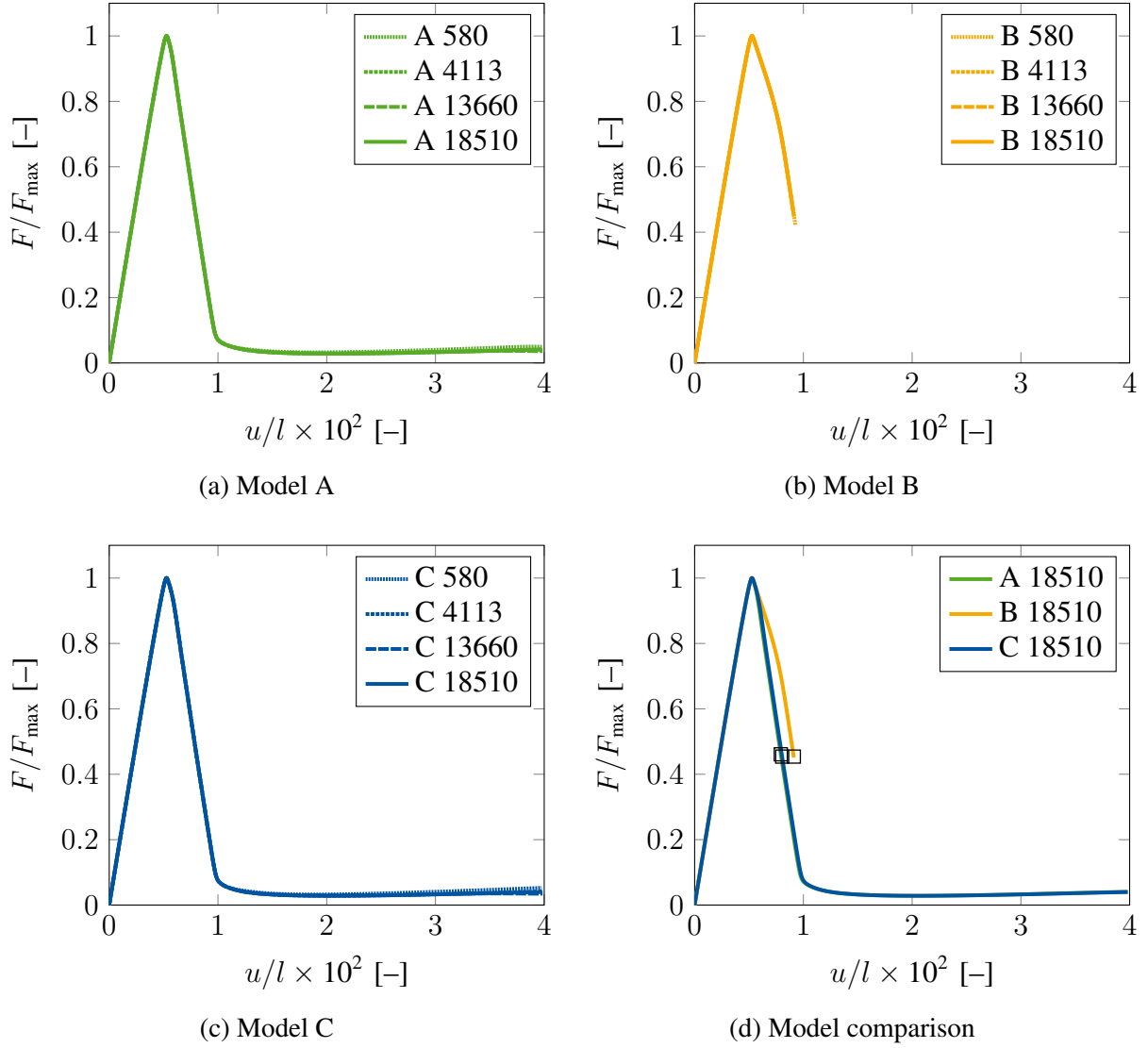


Figure 16: Mesh convergence studies for the three-dimensional tensile specimen and model comparison. The forces are normalized with respect to the maximum force of the finest mesh (18510 elements) of model B with  $F_{\max} = 1.1762 \times 10^4$  [N]. The black boxes in Fig. 16d indicate the points of comparison in Figs. 17 and 18.

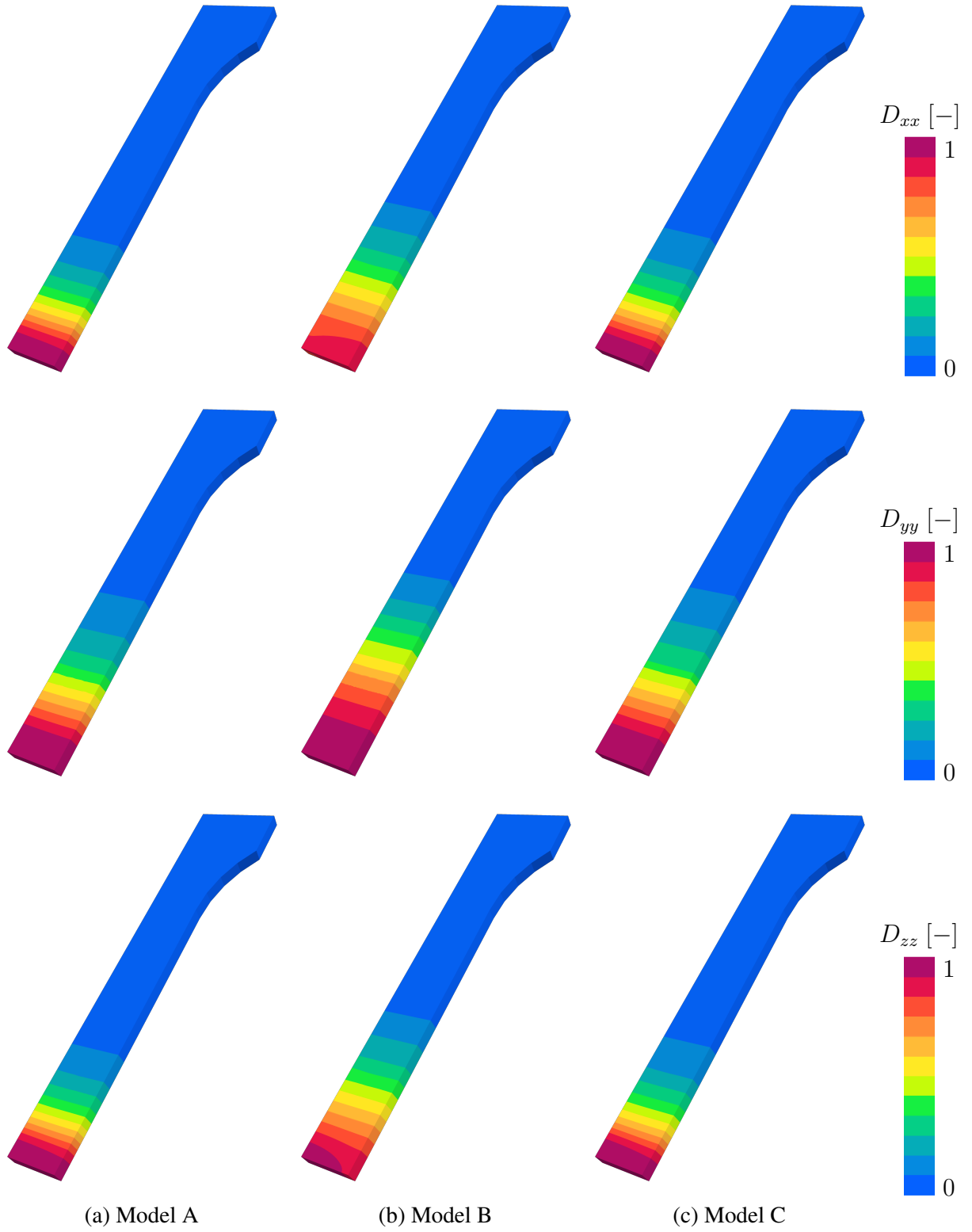


Figure 17: Contour plots of the normal components of the damage tensor for the three-dimensional tensile specimen at the point of comparison indicated in Fig. 16d.



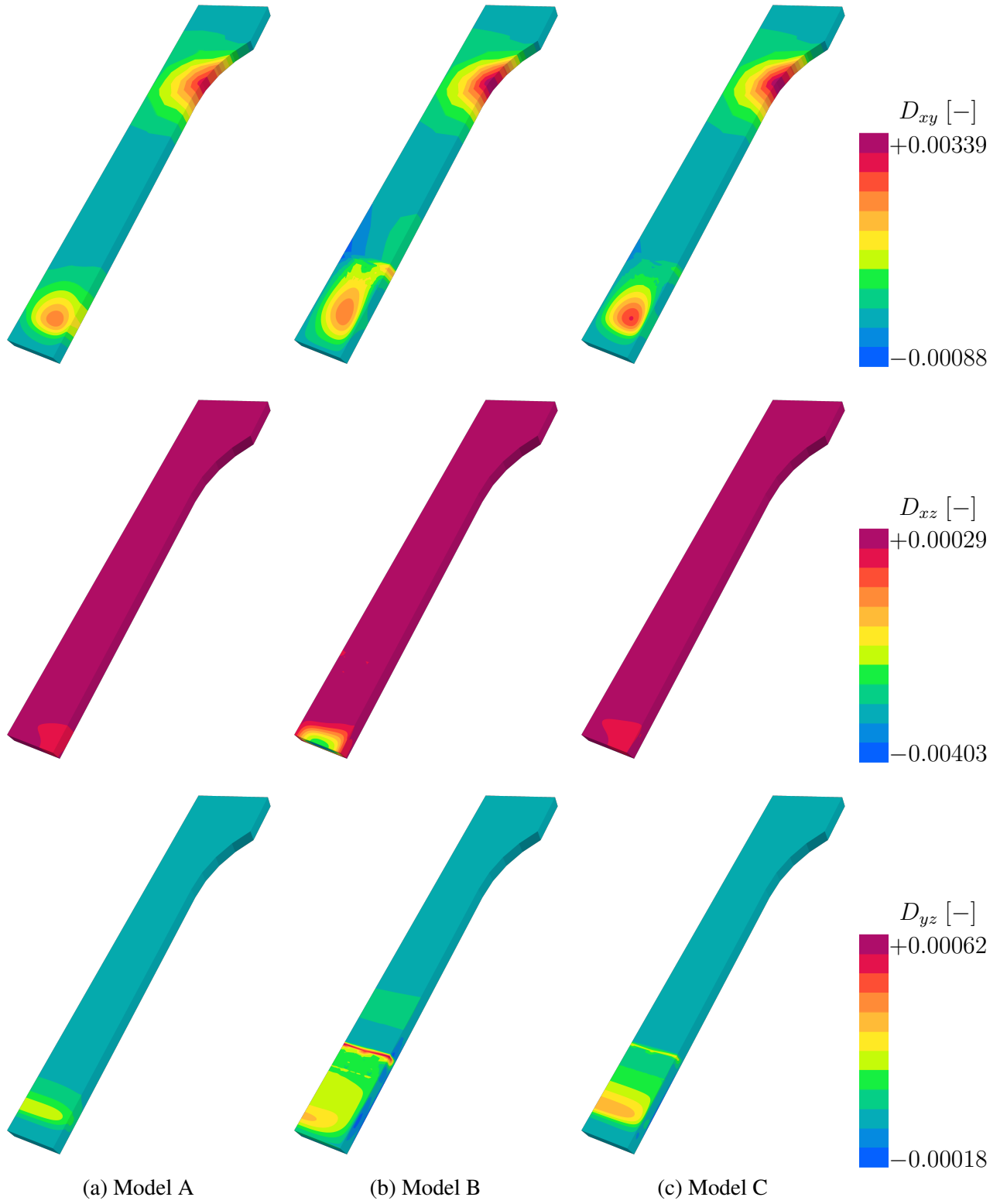


Figure 18: Contour plots of the shear components of the damage tensor for the three-dimensional tensile specimen at the point of comparison indicated in Fig. 16d.

#### 4.4 Smiley specimen

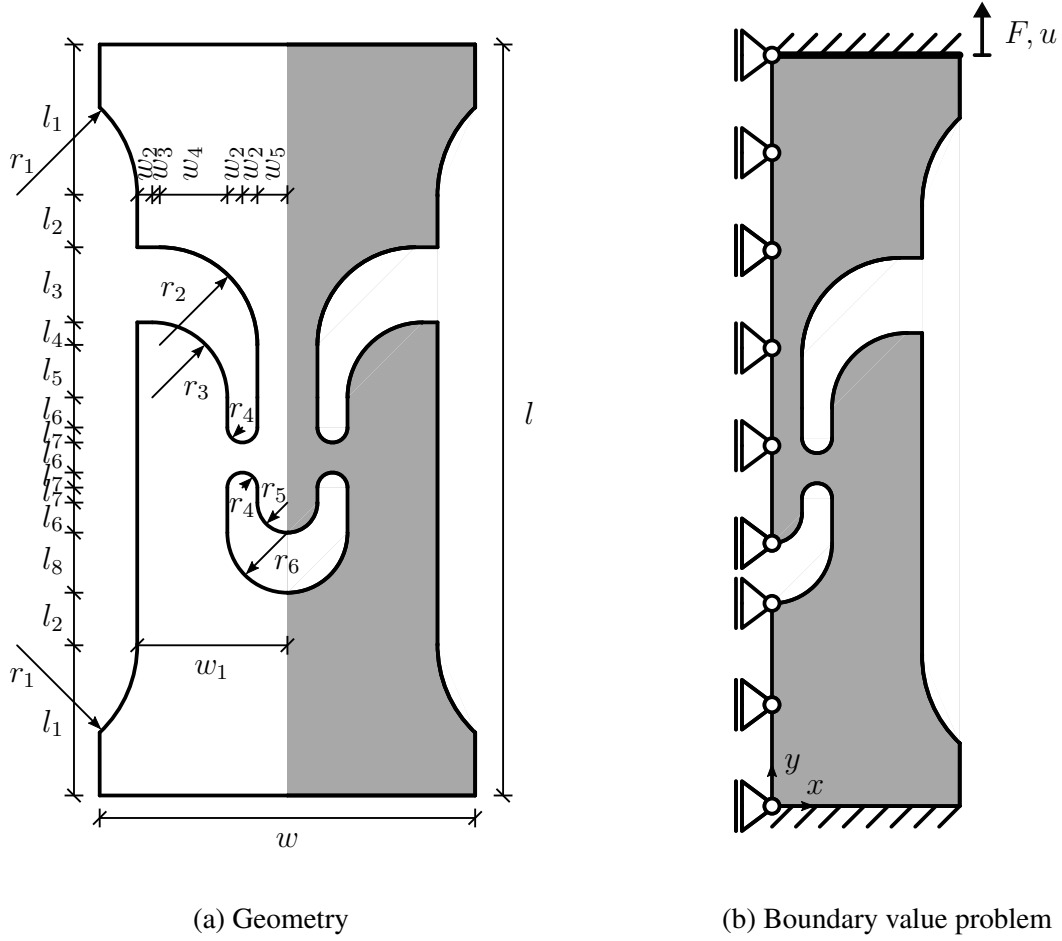


Figure 19: Geometry and boundary value problem of the smiley specimen.

The final example serves for the investigation of a complex combination of normal and shear stress states. Inspired by Gerke et al. [2020], Roth and Mohr [2016], Tancogne-Dejean et al. [2016], Till and Hackl [2013], and Miyauchi [1984], we designed a smiley specimen where the normal and shear load carrying cross sections are equal. The design, further, features smooth transitions from arcs to straight lines to avoid stress singularities at these points. Furthermore, this example illustrates the necessity to investigate the eigenvalues of the damage tensor in order to accurately study the degradation of the specimen and, again, compares the differing results of the isotropic and the anisotropic damage model.

Fig. 19 shows the geometry and the considered boundary value problem. The dimensions read  $l = 50$  [mm],  $l_1 = 10$  [mm],  $l_2 = 3.5$  [mm],  $l_3 = 5$  [mm],  $l_4 = 1.5$  [mm],  $l_5 = 4.5$  [mm],  $l_6 = 2$  [mm],  $l_7 = 1$  [mm],  $l_8 = 4$  [mm],  $w = 25$  [mm],  $w_1 = 10$  [mm],  $w_2 = 1$  [mm],  $w_3 = 0.5$  [mm],  $w_4 = 4.5$  [mm],  $w_5 = 2$  [mm],  $r_1 = 8$  [mm],  $r_2 = 6.5$  [mm],  $r_3 = 5$  [mm],  $r_4 = 1$  [mm],  $r_5 = 2$  [mm], and  $r_6 = 4$  [mm] with a thickness of 1 [mm]. Due to symmetry,

only one half of the specimen with clamped ends is modeled in the simulation. The internal length scales of model B are chosen as  $A_i^B = 75 \text{ [MPa mm}^2\text{]}$  and the parameters of model A and C are identified as  $A_i^A = 220 \text{ [MPa mm}^2\text{]}$  and  $A_i^C = 790 \text{ [MPa mm}^2\text{]}$ .

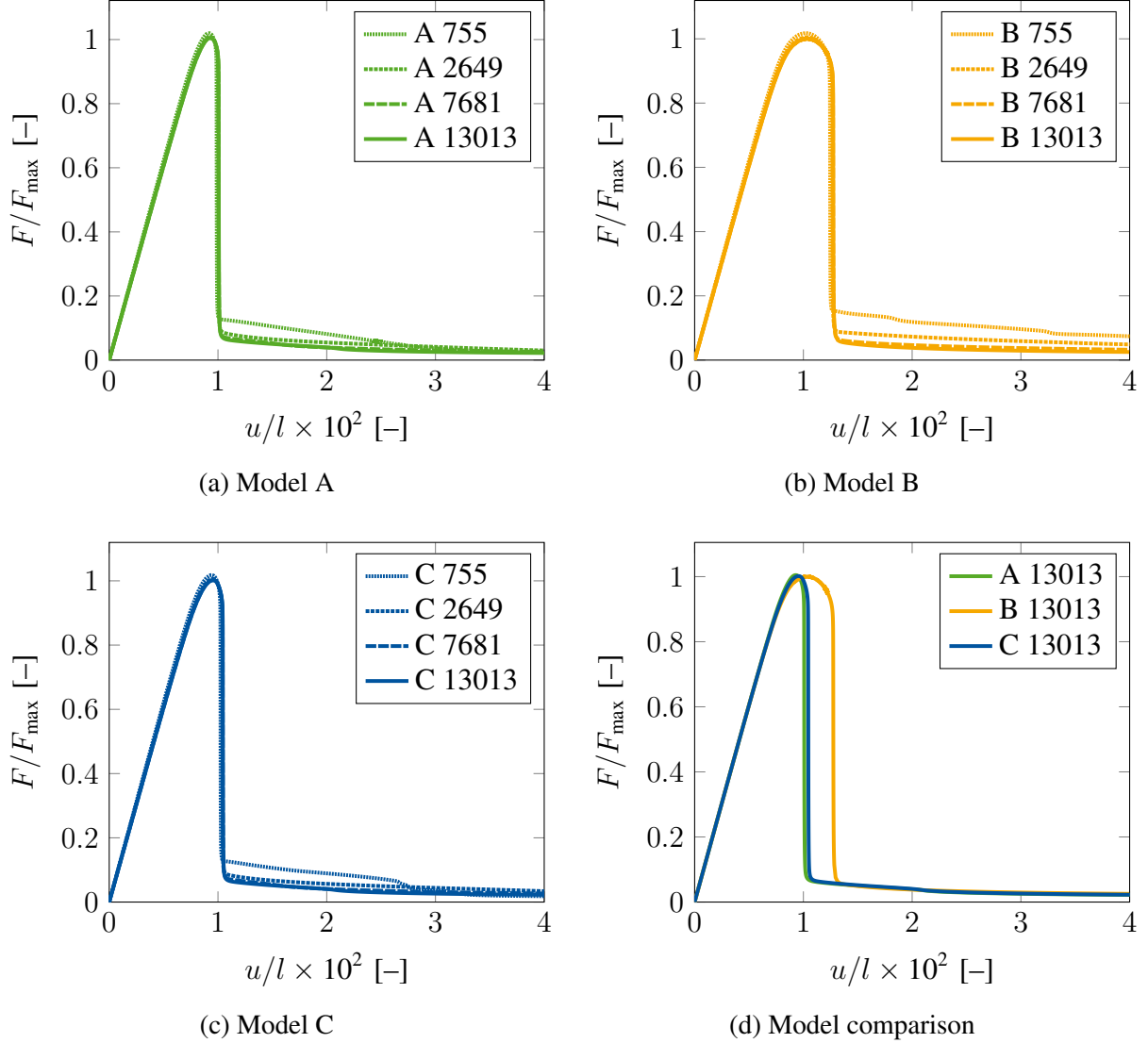


Figure 20: Mesh convergence studies for the smiley specimen and model comparison. The forces are normalized with respect to the maximum force of the finest mesh (13013 elements) of model B with  $F_{\max} = 2.9590 \times 10^3 \text{ [N]}$ .

Fig. 20 shows the normalized force-displacement curves. In this example, no model obtains convergence with respect to the maximum peak force using the coarsest mesh (755 elements), only upon mesh refinement this is achieved. The model comparison in Fig. 20d yields a distinct horizontal offset to the right of the vertical drop for model B at  $u_{0.5F_{\max}}^B/l \times 10^2 = 1.275 \text{ [-]}$ . For this example, a difference in the force drop can also be observed for models A and C with  $u_{0.5F_{\max}}^A/l \times 10^2 = 1.008 \text{ [-]}$  compared to  $u_{0.5F_{\max}}^C/l \times 10^2 = 1.045 \text{ [-]}$ .

The damage contour plots in Fig. 21 reveal a tension dominated failure with all models, where

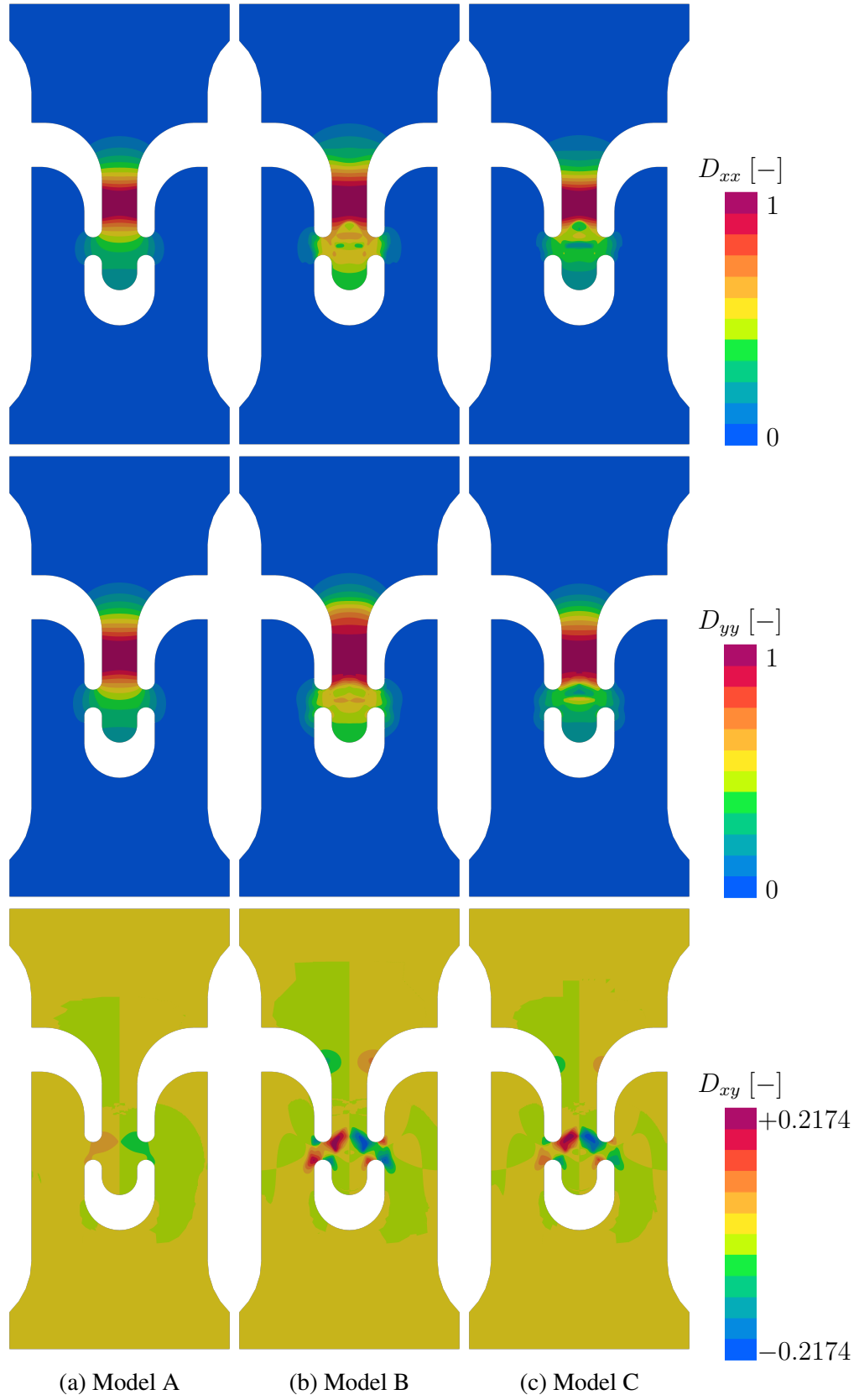


Figure 21: Contour plots of the normal and shear components of the damage tensor for the smiley specimen at the end of the simulation.

model B shows the largest damage zone. More models B and C exhibit concentrated peak values for the shear component of the damage tensor  $D_{xy}$  while model A yields a smooth distribution.

For the smiley specimen, we also study the evolution of the components of the damage tensor in Fig. 22, where we restrict ourselves to the presentation of model C. In the initial damage state, the normal component  $D_{xx}$  evolves equally at the tension and shear load carrying cross sections. In the intermediate damage states, the evolution of  $D_{xx}$  concentrates in the normal load carrying cross section up to total failure. The evolution of the normal component  $D_{yy}$  occurs predominantly in the normal load carrying cross section during the entire loading. Finally, the evolution of the shear component  $D_{xy}$  primarily happens at the inner side of the shear load carrying cross section.

Next, Fig.23 shows the mesh convergence of the components of the damage tensor, where we again restrict ourselves to the presentation of model C. As indicated by the force-displacement curves in Fig. 20c, differences can be observed in the damage contour plots obtained with the coarsest mesh (Fig. 23a) compared to the results obtained with the refined meshes (Figs. 23b-23d). However, the results obtained with the refined meshes hardly deviate and are, thus, considered converged.

Now, we study the eigenvalues of the damage tensor for model C. Fig. 24 shows the first eigenvalue  $D_1$  (top) and second eigenvalue  $D_2$  (middle) as well as the scaled normals to the corresponding eigenvectors in the  $x$ - $y$ -plane. These normals are supposed to indicate the orientation and the density of the anisotropic micro cracks. Hence, the micro cracks associated with the largest eigenvalue  $D_1$  are perpendicular to the loading direction and exhibit the highest density in the completely damaged zone. Due to the orthogonality of eigenvectors and an in-plane loading, the micro cracks associated with the second eigenvalue  $D_2$  are perpendicular to the micro cracks associated with the first eigenvalue  $D_1$ .

Finally, Fig. 24 (bottom) shows the difference between the maximum of the normal components  $D_{xx}$ ,  $D_{yy}$ , and  $D_{zz}$  and the largest eigenvalue  $D_1$ . Evidently, a significant underestimation of the material degradation up to a value of  $-0.1926$  [—] occurs in the shear load dominated regions, when only considering the normal components of the Cartesian coordinate system.

The last study is concerned with the comparison of isotropic and anisotropic damage for the smiley specimen. Fig. 25 shows the normalized force-displacement curves for the isotropic and anisotropic models and for all models the isotropic formulation overestimates the maximum peak force (A: +4.52 [%], B: +9.49 [%], C: +7.65 [%]).

The corresponding isotropic damage contour plots are presented in Fig. 26 (top row) and, also for the isotropic models, total failure occurs in the tension load carrying cross section. However, the absolute difference of the isotropic damage value to the normals components of the damage tensor for the anisotropic computation (see Fig. 26 (middle and bottom row)) amounts up to

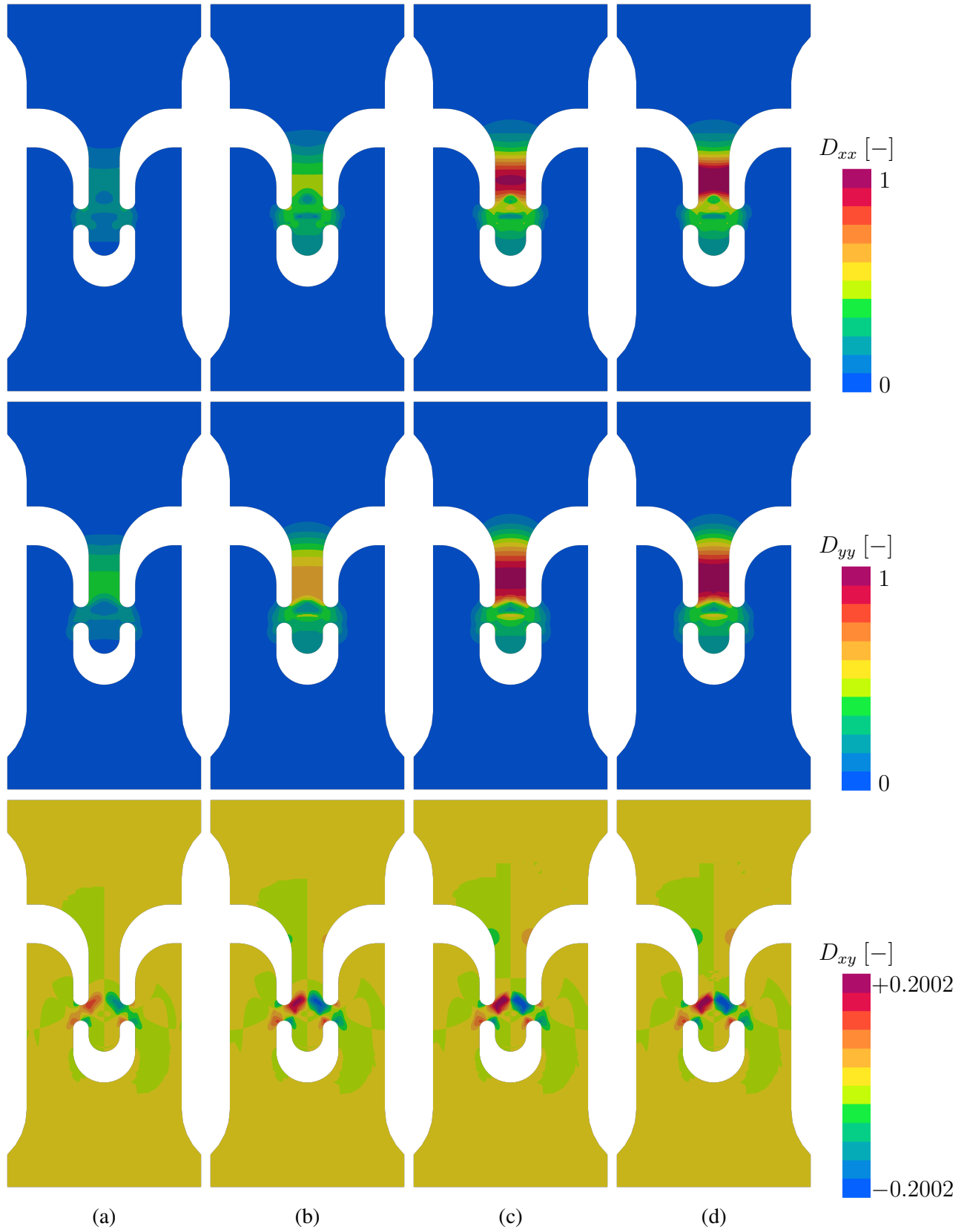


Figure 22: Contour plots of the evolution of the normal and shear components of the damage tensor for the smiley specimen (model C).

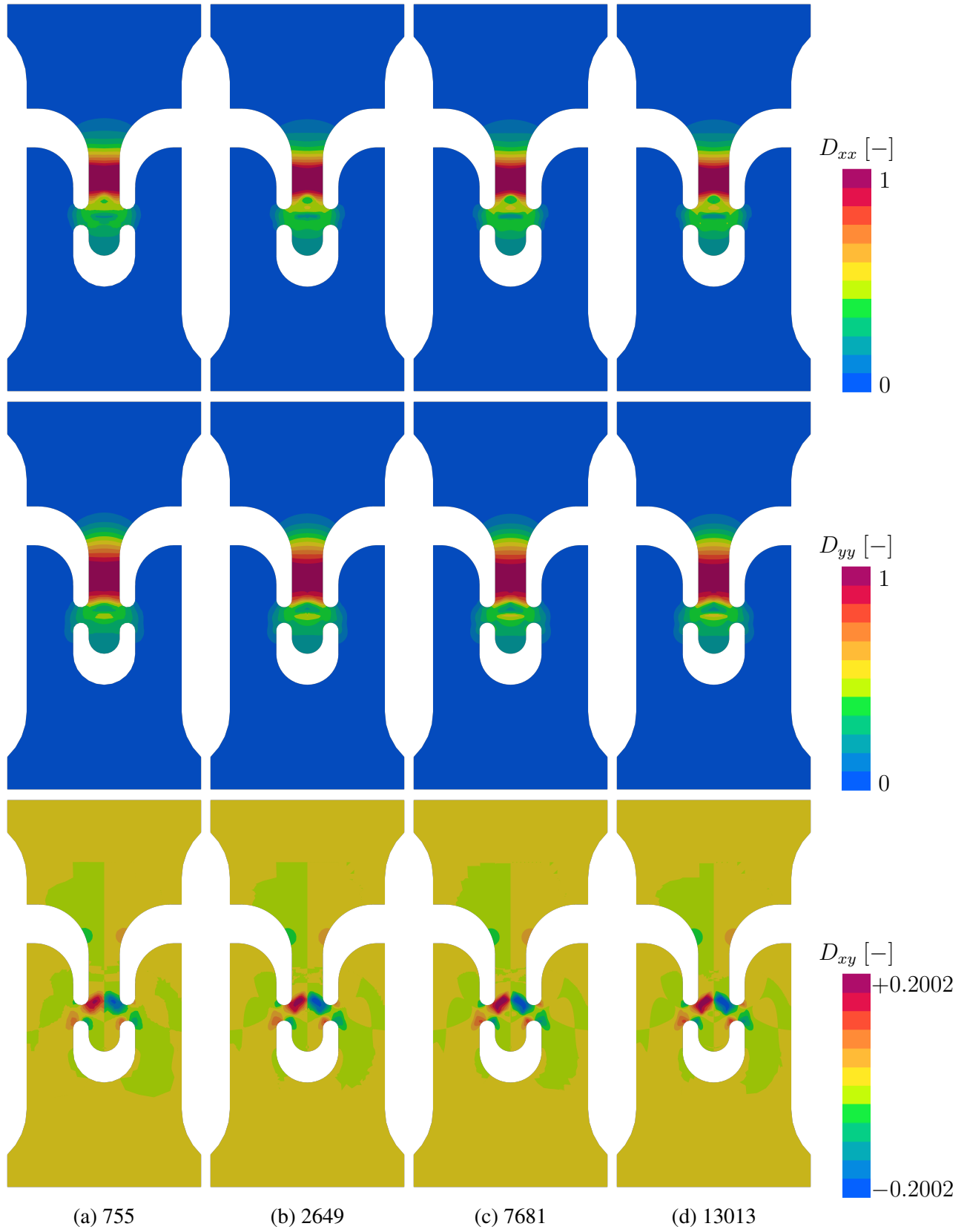


Figure 23: Mesh convergence study of the damage contour plots of the normal and shear components of the damage tensor for the smiley specimen at the end of the simulation (model C).

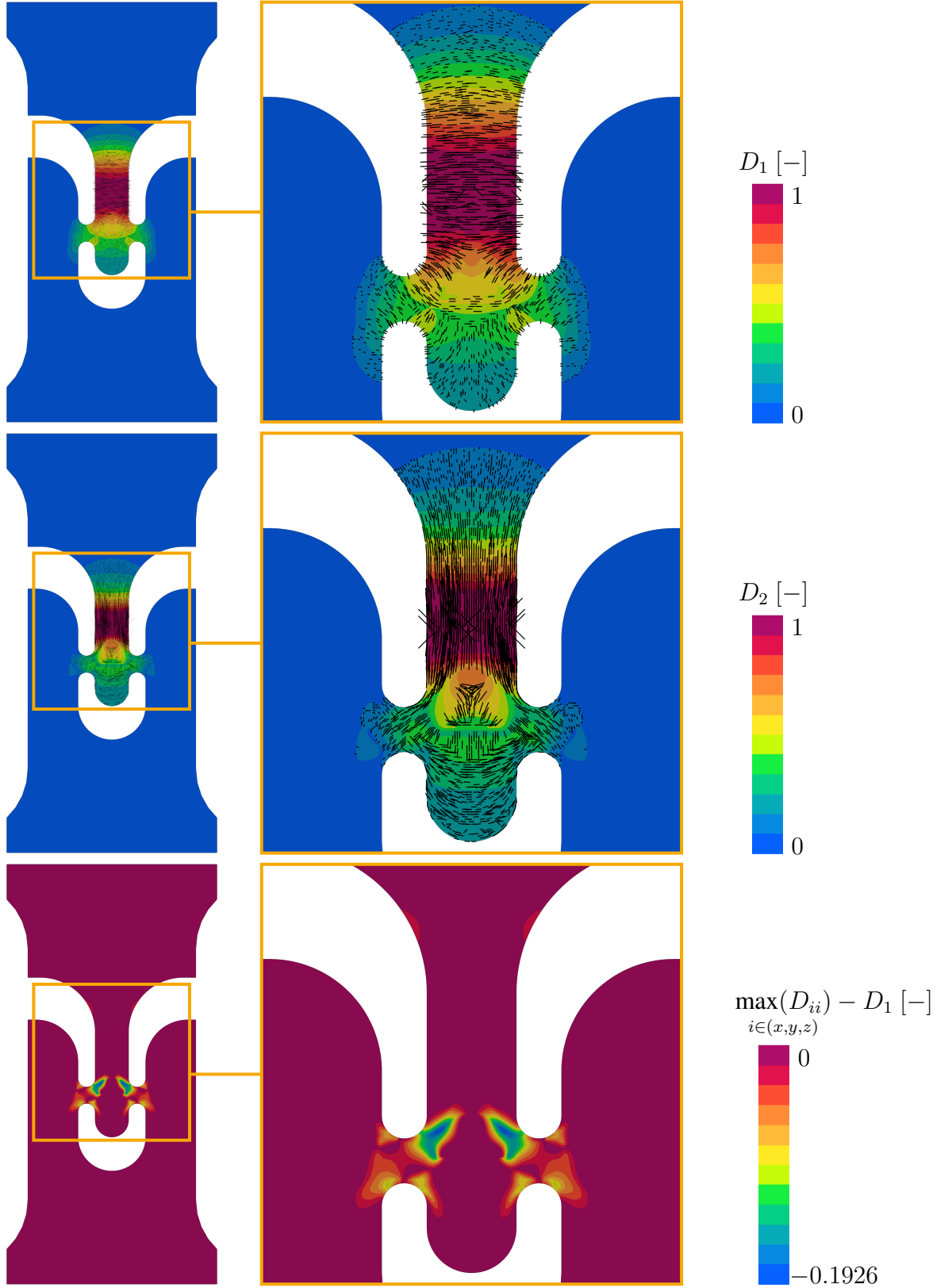


Figure 24: Contour plots of the first and second eigenvalue of the damage tensor and of the absolute difference between the maximum normal component and the first eigenvalue for the smiley specimen at the end of the simulation (model C). The black lines indicate the scaled normals to the first (top) and second eigenvector (middle) of the damage tensor.



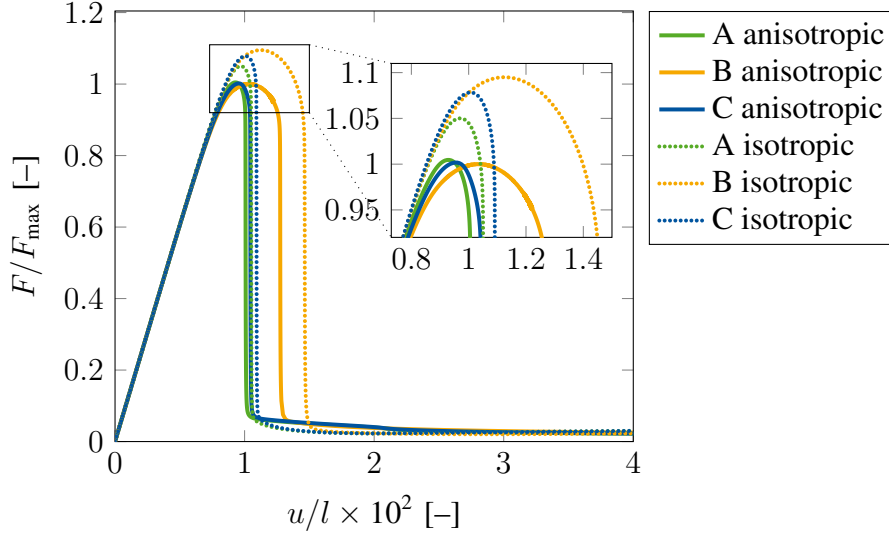


Figure 25: Comparison of the anisotropic and isotropic computation for the smiley specimen (13013 elements). The forces are normalized with respect to the maximum force of the anisotropic computation of model B with  $F_{\max} = 2.9590 \times 10^3$  [N].

0.4158  $[-]$  for  $|D - D_{xx}|$  and to 0.3293  $[-]$  for  $|D - D_{yy}|$ , which is in line with the observations in Fig. 25.

Last, the absolute difference of the isotropic damage value and the largest eigenvalue of the damage tensor for the anisotropic calculation for model C is shown in Fig. 27. The value of  $|D - D_1|$  reaches up to 0.1581  $[-]$  and, thus, underlines the significant difference between isotropic and anisotropic damage.

## Summary of the numerical results

The following most important results were obtained for model A (full regularization, six micromorphic degrees of freedom), model B (reduced regularization, three micromorphic degrees of freedom), and model C (reduced regularization, two micromorphic degrees of freedom) in the numerical examples:

- Models A, B and C effectively prevent localization in the structural force-displacement response (Figs. 2, 11, 16, and 20).
- Models A and C coincide in the structural response, while model B yields a higher energy dissipation and a horizontal offset of the vertical force drop to the right for the same maximum peak load (Figs. 2d, 11d, 16d, and 20d).
- Models A and C prevent localization of the normal and shear components of the damage tensor (Figs. 3a, 3c, 12a, 12c, 17a, 17c, 18a, 18c, 21a, and 21c). Model B also prevents

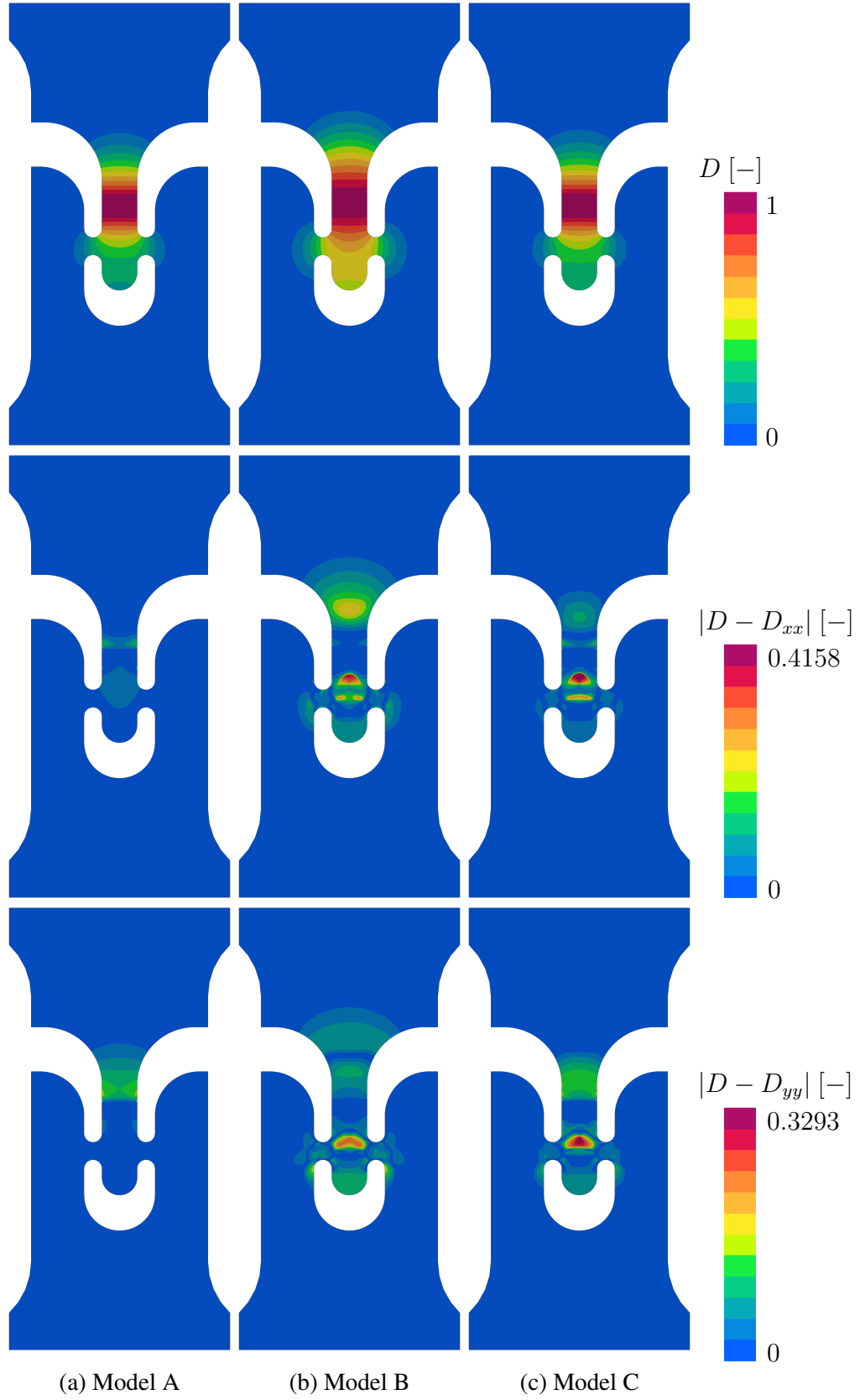


Figure 26: Contour plots of the isotropic damage value and its absolute difference to the normal components of the damage tensor for the smiley specimen at the end of the simulation.

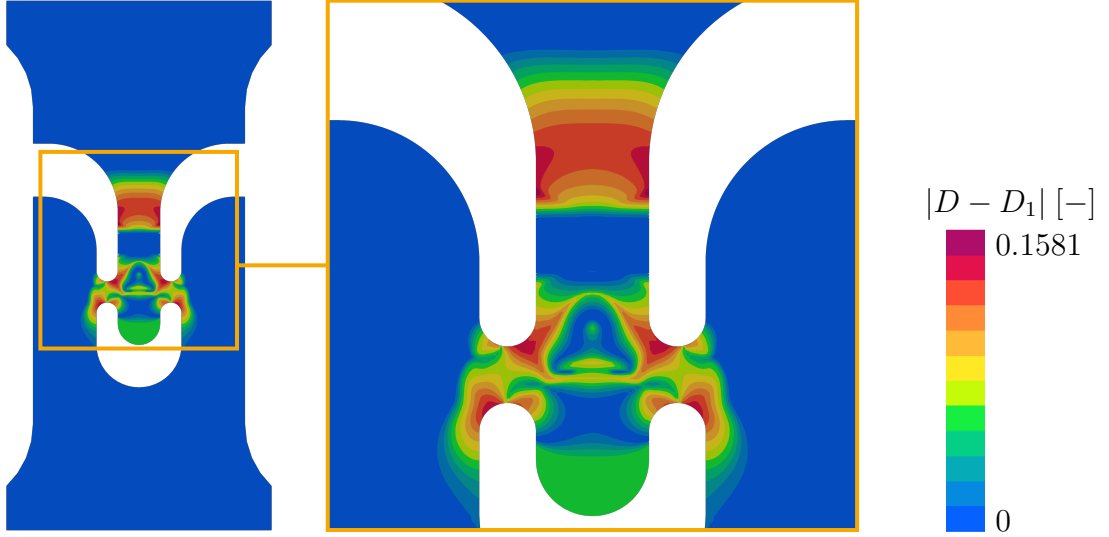


Figure 27: Contour plot of the absolute difference between the isotropic damage value and the first eigenvalue of the damage tensor for the smiley specimen at the end of the simulation (model C).

localization of the normal components of the damage tensor (Figs. 3b, 12b, 17b, and 21b), but a localization of one shear component occurred in a single example (Fig. 18b).

- The damage zones obtained with model B are thicker and, thus, dissipate more energy than the damage zones obtained with models A and C (Figs. 3, 12, 17, and 21).
- The consideration of isotropic damage continuously yields an overestimation of the structure's load bearing capacity (Figs. 4, 13, and 25).
- The influence of the artificial viscosity on the regularization, the structural response, and the damage distribution is ruled out (Figs. 6, 7, 8, 9, and 14).

## 5 Conclusion

This work investigated different gradient-extensions for tensor-valued internal variable based inelastic material models. Here, we specifically focused on the regularization of anisotropic damage at finite strains through a micromorphic gradient-extension of the damage driving force. Three different gradient-extensions with full (six micromorphic degrees of freedom) and reduced regularization (three and two micromorphic degrees of freedom) of the damage tensor were compared theoretically and numerically in the present study.

A high level of agreement was obtained between the results of the model with full regularization of all six independent components of the damage tensor and the model with a reduced regularization of the volumetric and deviatoric part of the damage tensor, which only utilizes

two micromorphic degrees of freedom. Thereby, an efficient, yet effective, regularization for anisotropic damage at finite strains was identified.

The utilized anisotropic damage model features a flexible formulation that incorporates isotropic, kinematic, and distortional damage hardening and fulfills the damage growth criterion for finite strains. Therefore, it can be considered as a general inelastic local material model of a tensor-valued internal variable based formulation.

Further investigations should verify the numerical results by experimental validations and could apply the gradient-extensions to the regularization of other inelastic localizing phenomena.

## Acknowledgements

Funding granted by the German Research Foundation (DFG) for projects number 453715964 (RE 1057/51-1), 417002380 (CRC 280 - A01) and 453596084 (CRC 339 - B05) is gratefully acknowledged.

## References

- Abatour, M. and Forest, S. [2023], ‘Strain gradient plasticity based on saturating variables’, *European Journal of Mechanics - A/Solids* p. 105016.
- Abatour, M., Forest, S., Ammar, K., Ovalle, C., Osipov, N. and Quilici, S. [2023], ‘Toward robust scalar-based gradient plasticity modeling and simulation at finite deformations’, *Acta Mechanica* **234**, 911–958.
- Ahrens, J., Geveci, B. and Law, C. [2005], ParaView: An end-user tool for large data visualization, in ‘Visualization Handbook’, Elsevier. ISBN 978-0123875822.
- Aldakheel, F., Hudobivnik, B. and Wriggers, P. [2019], ‘Virtual element formulation for phase-field modeling of ductile fracture’, *International Journal for Multiscale Computational Engineering* **17**(2), 181–200.
- Ambati, M., Kruse, R. and De Lorenzis, L. [2016], ‘A phase-field model for ductile fracture at finite strains and its experimental verification’, *Computational Mechanics* **57**, 149–167.
- Bažant, Z. P. and Jirásek, M. [2002], ‘Nonlocal integral formulations of plasticity and damage: Survey of progress’, *Journal of Engineering Mechanics* **128**(11), 1119–1149.
- Bažant, Z. P. and Pijaudier-Cabot, G. [1988], ‘Nonlocal Continuum Damage, Localization Instability and Convergence’, *Journal of Applied Mechanics* **55**(2), 287–293.

- Badreddine, H., Saanouni, K. and Nguyen, T. D. [2015], ‘Damage anisotropy and its effect on the plastic anisotropy evolution under finite strains’, *International Journal of Solids and Structures* **63**, 11–31.
- Barfusz, O., Brepols, T., van der Velden, T., Frischkorn, J. and Reese, S. [2021a], ‘A single gauss point continuum finite element formulation for gradient-extended damage at large deformations’, *Computer Methods in Applied Mechanics and Engineering* **373**, 113440.
- Barfusz, O., van der Velden, T., Brepols, T., Holthusen, H. and Reese, S. [2021b], ‘A reduced integration-based solid-shell finite element formulation for gradient-extended damage’, *Computer Methods in Applied Mechanics and Engineering* **382**, 113884.
- Barfusz, O., van der Velden, T., Brepols, T. and Reese, S. [2022], ‘Gradient-extended damage analysis with reduced integration-based solid-shells at large deformations’, *Computer Methods in Applied Mechanics and Engineering* **389**, 114317.
- Brepols, T., Wulfinghoff, S. and Reese, S. [2017], ‘Gradient-extended two-surface damage-plasticity: Micromorphic formulation and numerical aspects’, *International Journal of Plasticity* **97**, 64 – 106.
- Brepols, T., Wulfinghoff, S. and Reese, S. [2020], ‘A gradient-extended two-surface damage-plasticity model for large deformations’, *International Journal of Plasticity* **129**, 102635.
- Carol, I., Bažant, Z. P. and Prat, P. C. [1991], ‘Geometric damage tensor based on microplane model’, *Journal of Engineering Mechanics* **117**(10), 2429–2448.
- Carol, I., Rizzi, E. and Willam, K. [2002], ‘An ‘extended’ volumetric/deviatoric formulation of anisotropic damage based on a pseudo-log rate’, *European Journal of Mechanics - A/Solids* **21**(5), 747–772.
- Challamel, N., Lanos, C. and Casandjian, C. [2005], ‘Strain-based anisotropic damage modelling and unilateral effects’, *International Journal of Mechanical Sciences* **47**(3), 459–473.
- Coleman, B. D. and Noll, W. [1961], ‘Foundations of linear viscoelasticity’, *Reviews of modern physics* **33**, 239–249.
- de Borst, R., Benallal, A. and Heeres, O. [1996], ‘A gradient-enhanced damage approach to fracture’, *Journal de Physique IV* **6**, 491–502.
- de Borst, R., Pamin, J. and Geers, M. [1999], ‘On coupled gradient-dependent plasticity and damage theories with a view to localization analysis’, *European Journal of Mechanics - A/Solids* **18**(6), 939–962.
- Desmorat, R. [2016], ‘Anisotropic damage modeling of concrete materials’, *International Journal of Damage Mechanics* **25**(6), 818–852.

- Desmorat, R., Gatuingt, F. and Ragueneau, F. [2007], ‘Nonlocal anisotropic damage model and related computational aspects for quasi-brittle materials’, *Engineering Fracture Mechanics* **74**(10), 1539–1560.
- Dimitrijevic, B. J. and Hackl, K. [2008], ‘A method for gradient enhancement of continuum damage models’, *Technische Mechanik-European Journal of Engineering Mechanics* **28**(1), 43–52.
- Dimitrijevic, B. J. and Hackl, K. [2011], ‘A regularization framework for damage–plasticity models via gradient enhancement of the free energy’, *International Journal for Numerical Methods in Biomedical Engineering* **27**(8), 1199–1210.
- Dittmann, M., Aldakheel, F., Schulte, J., Schmidt, F., Krüger, M., Wriggers, P. and Hesch, C. [2020], ‘Phase-field modeling of porous-ductile fracture in non-linear thermo-elasto-plastic solids’, *Computer Methods in Applied Mechanics and Engineering* **361**, 112730.
- Dorn, C. and Wulfinghoff, S. [2021], ‘A gradient-extended large-strain anisotropic damage model with crack orientation director’, *Computer Methods in Applied Mechanics and Engineering* **387**, 114123.
- Fassin, M., Eggersmann, R., Wulfinghoff, S. and Reese, S. [2019a], ‘Efficient algorithmic incorporation of tension compression asymmetry into an anisotropic damage model’, *Computer Methods in Applied Mechanics and Engineering* **354**, 932–962.
- Fassin, M., Eggersmann, R., Wulfinghoff, S. and Reese, S. [2019b], ‘Gradient-extended anisotropic brittle damage modeling using a second order damage tensor – theory, implementation and numerical examples’, *International Journal of Solids and Structures* **167**, 93–126.
- Felder, S., Kopic-Osmanovic, N., Holthusen, H., Brepols, T. and Reese, S. [2022], ‘Thermo-mechanically coupled gradient-extended damage-plasticity modeling of metallic materials at finite strains’, *International Journal of Plasticity* **148**, 103142.
- Forest, S. [2009], ‘Micromorphic approach for gradient elasticity, viscoplasticity, and damage’, *Journal of Engineering Mechanics* **135**(3), 117–131.
- Forest, S. [2016], ‘Nonlinear regularization operators as derived from the micromorphic approach to gradient elasticity, viscoplasticity and damage’, *Proceedings of the Royal Society A: Mathematical, Physical and Engineering Sciences* **472**(2188), 20150755.
- Friedlein, J., Mergheim, J. and Steinmann, P. [2021], ‘A finite plasticity gradient-damage model for sheet metals during forming and clinching’, *Key Engineering Materials* **883**, 57–64.
- Friedlein, J., Mergheim, J. and Steinmann, P. [2023], ‘Efficient gradient enhancements for plasticity with ductile damage in the logarithmic strain space’, *European Journal of Mechanics - A/Solids* **99**, 104946.

- Geers, M. G. D., Brekelmans, W. A. M. and de Borst, R. [1994], ‘Viscous regularization of strain-localisation for damaging materials’, *DIANA Computational Mechanics ‘94* pp. 127–138.
- Gerke, S., Zistl, M. and Brünig, M. [2020], ‘Experiments and numerical simulation of damage and fracture of the x0-specimen under non-proportional loading paths’, *Engineering Fracture Mechanics* **224**, 106795.
- Hansen, N. and Schreyer, H. [1994], ‘A thermodynamically consistent framework for theories of elastoplasticity coupled with damage’, *International Journal of Solids and Structures* **31**(3), 359–389.
- Hegde, M. and Mulay, S. S. [2022], ‘Evolving structural tensor approach to model the damage induced anisotropy in viscoelastic solids’, *International Journal of Solids and Structures* **248**, 111655.
- Holthusen, H., Brepols, T., Reese, S. and Simon, J.-W. [2020], ‘An anisotropic constitutive model for fiber-reinforced materials including gradient-extended damage and plasticity at finite strains’, *Theoretical and Applied Fracture Mechanics* **108**, 102642.
- Holthusen, H., Brepols, T., Reese, S. and Simon, J.-W. [2022a], ‘A two-surface gradient-extended anisotropic damage model using a second order damage tensor coupled to additive plasticity in the logarithmic strain space’, *Journal of the Mechanics and Physics of Solids* **163**, 104833.
- Holthusen, H., Brepols, T., Simon, J.-W. and Reese, S. [2022b], A gradient-extended anisotropic damage-plasticity model in the logarithmic strain space, in ‘ECCOMAS Congress 2022-8th European Congress on Computational Methods in Applied Sciences and Engineering’, pp. 1–12.
- Holthusen, H., Lamm, L., Brepols, T., Reese, S. and Kuhl, E. [2023], ‘Theory and implementation of inelastic constitutive artificial neural networks’, *arXiv* .  
**URL:** <https://doi.org/10.48550/arXiv.2311.06380>
- HyperWorks [2022], ‘Hypermesh’, *Altair Engineering, Inc.* .  
**URL:** <https://altairhyperworks.com/product/HyperMesh>
- Javili, A., McBride, A. T. and Steinmann, P. [2021], ‘A geometrically exact formulation of peridynamics’, *Theoretical and Applied Fracture Mechanics* **111**, 102850.
- Jebahi, M. and Forest, S. [2021], ‘Scalar-based strain gradient plasticity theory to model size-dependent kinematic hardening effects’, *Continuum Mechanics and Thermodynamics* **33**, 1223–1245.

- Jirásek, M. and Suárez, F. [2016], ‘Localization properties of desmorat’s anisotropic damage model’, *Computers & Structures* **174**, 139–153.
- Kiefer, B., Waffenschmidt, T., Sprave, L. and Menzel, A. [2018], ‘A gradient-enhanced damage model coupled to plasticity—multi-surface formulation and algorithmic concepts’, *International Journal of Damage Mechanics* **27**(2), 253–295.
- Kikis, G., Ambati, M., De Lorenzis, L. and Klinkel, S. [2021], ‘Phase-field model of brittle fracture in reissner–mindlin plates and shells’, *Computer Methods in Applied Mechanics and Engineering* **373**, 113490.
- Korelc, J. [2002], ‘Multi-language and multi-environment generation of nonlinear finite element codes’, *Multi-language and Multi-environment Generation of Nonlinear Finite Element Codes* **18**, 312–327.
- Korelc, J. and Wriggers, P. [2016], *Automation of Finite Element Methods*, Springer.
- Kuhl, E., Ramm, E. and de Borst, R. [2000], ‘An anisotropic gradient damage model for quasi-brittle materials’, *Computer Methods in Applied Mechanics and Engineering* **183**(1), 87–103.
- Langenfeld, K., Junker, P. and Mosler, J. [2018], ‘Quasi-brittle damage modeling based on incremental energy relaxation combined with a viscous-type regularization’, *Continuum Mechanics and Thermodynamics* **30**(5), 1125–1144.
- Langenfeld, K., Kurzeja, P. and Mosler, J. [2022], ‘How regularization concepts interfere with (quasi-)brittle damage: a comparison based on a unified variational framework’, *Continuum Mechanics and Thermodynamics* **34**, 1517–1544.
- Langenfeld, K. and Mosler, J. [2020], ‘A micromorphic approach for gradient-enhanced anisotropic ductile damage’, *Computer Methods in Applied Mechanics and Engineering* **360**, 112717.
- Laurien, M., Javili, A. and Steinmann, P. [2023], ‘Peridynamic modeling of nonlocal degrading interfaces in composites’, *Forces in Mechanics* **10**, 100124.
- Lemaitre, J., Desmorat, R. and Sauzay, M. [2000], ‘Anisotropic damage law of evolution’, *European Journal of Mechanics - A/Solids* **19**(2), 187–208.
- Leukart, M. and Ramm, E. [2003], ‘A comparison of damage models formulated on different material scales’, *Computational Materials Science* **28**(3), 749–762.
- Menzel, A., Ekh, M., Steinmann, P. and Runesson, K. [2002], ‘Anisotropic damage coupled to plasticity: Modelling based on the effective configuration concept’, *International Journal for Numerical Methods in Engineering* **54**(10), 1409–1430.



- Miehe, C., Apel, N. and Lambrecht, M. [2002], ‘Anisotropic additive plasticity in the logarithmic strain space: modular kinematic formulation and implementation based on incremental minimization principles for standard materials’, *Computer Methods in Applied Mechanics and Engineering* **191**(47), 5383–5425.
- Miyauchi, K. [1984], ‘A proposal for a planar simple shear test in sheet metals’, *Scientific Papers of the Institute of Physical and Chemical Research (Japan)* **78**(3), 27 – 40.
- Needleman, A. [1988], ‘Material rate dependence and mesh sensitivity in localization problems’, *Computer Methods in Applied Mechanics and Engineering* **67**(1), 69–85.
- Niazi, M. S., Wisselink, H. H. and Meinders, T. [2013], ‘Viscoplastic regularization of local damage models: revisited’, *Computational Mechanics* **51**, 203–216.
- Peerlings, R. H. J., de Borst, R., Brekelmans, W. A. M. and de Vree, J. H. P. [1996], ‘Gradient enhanced damage for quasi-brittle materials’, *International Journal for Numerical Methods in Engineering* **39**(19), 3391–3403.
- Pijaudier-Cabot, G. and Bazant, Z. P. [1987], ‘Nonlocal damage theory’, *Journal of Engineering Mechanics* **113**(10), 1512–1533.
- Poggenpohl, L., Brepols, T., Holthusen, H., Wulfinghoff, S. and Reese, S. [2021], ‘Towards brittle damage in carbon fiber reinforced plastics: A gradient extended approach’, *Composite Structures* **255**, 112911.
- Poggenpohl, L., Holthusen, H. and Simon, J.-W. [2022], ‘Failure zone homogenization for modeling damage- and debonding-induced softening in composites including gradient-extended damage at finite strains’, *International Journal of Plasticity* **154**, 103277.
- Poh, L., Peerlings, R., Geers, M. and Swaddiwudhipong, S. [2011], ‘An implicit tensorial gradient plasticity model – formulation and comparison with a scalar gradient model’, *International Journal of Solids and Structures* **48**(18), 2595–2604.
- Reese, S., Brepols, T., Fassin, M., Poggenpohl, L. and Wulfinghoff, S. [2021], ‘Using structural tensors for inelastic material modeling in the finite strain regime – a novel approach to anisotropic damage’, *Journal of the Mechanics and Physics of Solids* **146**, 104174.
- Roth, C. C. and Mohr, D. [2016], ‘Ductile fracture experiments with locally proportional loading histories’, *International Journal of Plasticity* **79**, 328–354.
- Sarkar, S., Singh, I. and Mishra, B. [2020], ‘A thermo-mechanical gradient enhanced damage method for fracture’, *Computational Mechanics* **66**, 1399–1426.

- Schütte, H. and Bruhns, O. [2002], ‘On a geometrically nonlinear damage model based on a multiplicative decomposition of the deformation gradient and the propagation of microcracks’, *Journal of the Mechanics and Physics of Solids* **50**(4), 827–853.
- Silling, S. [2000], ‘Reformulation of elasticity theory for discontinuities and long-range forces’, *Journal of the Mechanics and Physics of Solids* **48**(1), 175–209.
- Simo, J. [1987], ‘On a fully three-dimensional finite-strain viscoelastic damage model: Formulation and computational aspects’, *Computer Methods in Applied Mechanics and Engineering* **60**(2), 153–173.
- Sprave, L. and Menzel, A. [2020], ‘A large strain gradient-enhanced ductile damage model: finite element formulation, experiment and parameter identification’, *Acta Mechanica* **231**, 5159–5192.
- Sprave, L. and Menzel, A. [2023], ‘A large strain anisotropic ductile damage model — effective driving forces and gradient-enhancement of damage vs. plasticity’, *Computer Methods in Applied Mechanics and Engineering* **416**, 116284.
- Steif, P., Spaepen, F. and Hutchinson, J. [1982], ‘Strain localization in amorphous metals’, *Acta Metallurgica* **30**(2), 447–455.
- Tancogne-Dejean, T., Roth, C. C., Woy, U. and Mohr, D. [2016], ‘Probabilistic fracture of ti-6al-4v made through additive layer manufacturing’, *International Journal of Plasticity* **78**, 145–172.
- Taylor, R. L. and Govindjee, S. [2020], ‘FEAP - - a finite element analysis program’, *University of California, Berkeley* .  
**URL:** [http://projects.ce.berkeley.edu/feap/manual\\_86.pdf](http://projects.ce.berkeley.edu/feap/manual_86.pdf)
- Till, E. and Hackl, B. [2013], Calibration of plasticity - and failure models for ahss sheets, in ‘Towards Zero Failure Production Methods by Advanced Modeling Techniques and a Process Integrated Virtual Control, IDDRG, International Deep Drawing Research Group Conference, 2013’, pp. 119–124.
- van der Velden, T., Ritzert, S., Reese, S. and Waimann, J. [2023], ‘A novel numerical strategy for modeling the moving boundary value problem of electrochemical machining’, *International Journal for Numerical Methods in Engineering* **124**(8), 1856–1882.
- van der Velden, T., Rommes, B., Klink, A., Reese, S. and Waimann, J. [2021], ‘A novel approach for the efficient modeling of material dissolution in electrochemical machining’, *International Journal of Solids and Structures* **229**, 111106.
- Voyiadjis, G. Z. and Park, T. [1999], ‘The kinematics of damage for finite-strain elasto-plastic solids’, *International Journal of Engineering Science* **37**(7), 803–830.

- Wulfinghoff, S. and Böhlke, T. [2012], ‘Equivalent plastic strain gradient enhancement of single crystal plasticity: theory and numerics’, *Proceedings of the Royal Society A: Mathematical, Physical and Engineering Sciences* **468**(2145), 2682–2703.
- Wulfinghoff, S., Fassin, M. and Reese, S. [2017], ‘A damage growth criterion for anisotropic damage models motivated from micromechanics’, *International Journal of Solids and Structures* **121**, 21–32.
- Wulfinghoff, S., Forest, S. and Böhlke, T. [2015], ‘Strain gradient plasticity modeling of the cyclic behavior of laminate microstructures’, *Journal of the Mechanics and Physics of Solids* **79**, 1–20.